Doctoral Dissertation

Ionic Liquid-Based One-Pot Synthesis of Pt Metal/Alloy Nanoparticles Supported sp^2 Carbon Electrocatalysts for PEM Fuel Cells

Yu Yao

July 2020

Department of Applied Chemistry

Graduate School of Engineering,

Osaka University

Ionic Liquid-Based One-Pot Synthesis of Pt Metal/Alloy Nanoparticles Supported sp^2 Carbon Electrocatalysts for PEM Fuel Cells

（イオン液体を用いた白金ならびに白金合金ナノ粒子担持 sp^2 炭素材料の熱分解法によるワンポット作製）

2020

Yu Yao

Department of Applied Chemistry

Graduate School of Engineering

Osaka University

Preface

The works of this doctoral thesis were carried out under the guidance of Professor Dr. Susumu Kuwabata at Department of Applied Chemistry, Graduate School of Engineering, Osaka University during 2015-2020.

The object of this thesis is to develop the ionic liquid-based one-pot synthesis method for preparation of novel Pt or Pt-alloy nanoparticles-supported carbon catalyst toward oxygen reduction reaction with high catalytic activity and durability. It also involves the investigation of catalytic performance improvement of alloy nanoparticle-supported catalysts and alloy nanoparticle formation mechanism. The author wishes that the findings obtained in the work would contribute to progress science and technology in the field of ionic liquid and fuel cell catalyst.

Yu Yao

Department of Applied Chemistry,

Graduate School of Engineering,

Osaka University

Suita, Osaka,

Japan

July, 2020

Contents

General Introduction

Fuel cells are generally accepted as an ultimate energy solution for the high efficiency, zero emission, quiet operation process and unlimited renewable source of reactants.[1, 2] The launch of the hydrogen fuel cell vehicle "Mirai" from Toyota in November 2014 represented an excited landmark in the fuel cell arena. Presently, the major challenge in the research and development of the proton exchange membrane fuel cell (PEMFC) is to drastically improve the oxygen reduction reaction (ORR) at the cathode, the rate of which is much sluggish compared with the hydrogen oxidation reaction on anode.[3] Pt nanoparticle supported carbon materials is widely utilized as catalysts on cathode to enhance the reaction rate. Although many efforts have been made to fabricate Pt-free electro-catalysts, like non-precious transition metals,[4, 5] metal nitrides[6] and carbon-based metal-free electrocatalysts[7], it is rather difficult to apply these catalysts as commercially available ones for the fuel cell industry, due to their poor stability and limited performance toward ORR. Until now, Pt-based electrocatalysts have been the only option available for practical PEMFC because of their high catalytic activity and durability in acid.[8]

However, Pt nanoparticle-supported carbon electrocatalysts currently used for PEMFC still have several issues that need to be overcome, e.g. large overpotentials for the ORR, use of costly Pt, and insufficient durability. In order to address such issues, Pt-based binary and ternary electrocatalysts have recently been given much attention for the purpose of enhancing their catalytic activities and reducing their costs.[9] The commonly used elements for alloying are 3d transition metals, including Fe,[10, 11] Co,[12, 13] Cu,[14] and Ni,[15, 16] which can change the d-band center of the Pt nanoparticle that is closely related to the nature of the catalytic activity. Among them, Ni, which belongs to the same group of elements as Pt, is a promising element. Many studies have revealed that the higher activity of Pt-alloy catalysts results from the ligand

and strain effects.[17] Besides, Pt-alloy catalysts sometimes show excellent durability ascribed to the dealloying of the 3d transition non-noble metals.[13] This selective dissolution results in variation in the nanoparticle structure, i.e. a Pt-rich shell covering a Pt alloy core is formed. Rudi *et al.* also reported a systematic study on the enhancement of ORR activity by varying the Ni amount in the catalysts of the Pt_xNi_{1-x} series.[18]

In addition to the alloy nanoparticles, carbon supports also suffer from the corrosion, especially under some conditions such as start-up in fuel cell operation. The Pt nanoparticles subsequently agglomerate into larger particles, collapse into caves, and hence affect the long-term stability of the Pt catalyst.[19] The ideal carbon materials should possess a high surface area, excellent electronic conductivity, and chemical stability to disperse metal nanoparticles on uniformly. The sp^2-hybridized carbon materials such as carbon nanotubes (CNT) and graphene based materials (i.e. graphene nanoplatelets, GNPs) emerged as the promising candidates to replace the widely used carbon black as PEMFC catalyst supports for their unique physicochemical properties, including excellent electrical and thermal conductivities,[20, 21] high corrosion resistance,[22] and huge specific surface area.[23-25]

However, usually the sp^2 carbon support does not present a strong affinity towards catalyst particles without chemical pretreatment of the carbon support. To date, numerous approaches have been proposed for the preparation of noble metal nanoparticle-supporting sp^2-hybridized carbon composite materials for the ORR catalysis. These strategies can be roughly classified into five categories: electrodeposition,[26] electroless deposition,[27] nanoparticle modification onto functionalized carbon surface,[28] polymer wrapping method,[29] and physical methods.[30] Unfortunately, there is still plenty of room for improvement in each method for their practical use.

Almost a decade ago, Kuwabata and his colleagues reported that various metal nanoparticle-monodispersed ionic liquids (ILs) can be prepared by magnetron sputtering onto

the ILs.[31-35] Using these metal nanoparticle-monodispersed ILs, a two-step preparation method was developed for functional Pt-nanoparticle-supported carbon electrocatalysts with favorable catalytic activity and high durability for the ORR.[36, 37] They found that the thin IL layer serves to fixate the Pt nanoparticles onto the carbon materials like a glue and to improve the catalyst characteristics.[38-41]

The work of this doctoral thesis

Inspired by previous works mentioned above, I have made attempts to develop a one-pot pyrolysis method to produce sophisticated ORR electrocatalysts using IL mixtures consisting of IL, carbon supports, and thermally reducible Pt and/or Ni precursors. The final goal of this thesis is to synthesize Pt based nanoparrticle/sp^2 carbon catalyst with high catalytic activity and better durability by the IL based one-pot pyrolysis method. Stamenkovic *et al.* provided valuable experimental evidences showing that the unusual electronic structure at the d-band center position and the arrangement of atoms at the surface and near-surface regions in Pt_3Ni (111) improves the ORR activity.[42] The basic idea of this work is to use Ni as the alloy component for Pt nanoparticle and sp^2 carbon materials, like multi-walled carbon nanotube (MWCNT), as the carbon support. I expected by greatly use of the one-pot method and study the PtNi nanoparticle formation on MWCNTs, the influence of reaction conditions and precursors could be investigated in detail.

This thesis consists of three chapters as follows:

Chapter 1 describes the preparation of Pt/MWCNT and PtNi/MWCNTs with different precursors and precursor ratios using IL one-pot pyrolysis method. The electrocatalytic activity before and after durability test of the prepared catalysts were compared to understand the effect of Ni composition in nanoparticles on the ORR performance.

Chapter 2 describes the formation mechanism of PtNi alloy nanoparticle in PtNi/MWCNTs via a staircase heating process. PtNi/MWCNTs are obtained from two kinds of Ni precursors by the one-pot pyrolysis method. Their morphology, composition variation and electrochemical performance are reported to illustrate the growth mechanism of nanoparticles in this method.

Chapter 3 describes the application of hydrous insoluble Ni precursor in the PtNi/MWCNT preparation using the one-pot pyrolysis method. The Ni content and crystal structure of the resulting PtNi/MWCNT composites are confirmed. The effects of solubility and crystal water on the final formed PtNi/MWCNTs are investigated.

Chapter 1

Pt and PtNi nanoparticle-supported multi-walled carbon nanotube electrocatalysts prepared by one-pot pyrolytic synthesis with an ionic liquid

1-1. Introduction

Many studies have revealed that the higher activity of PtNi alloy catalysts results from the ligand and strain effects.[17, 43, 44] The ligand effect arises from the presence of neighboring Ni atom(s) to the Pt atom(s), which influences the electronic structure of the surface atoms on the PtNi alloy. On the other hand, the strain effect appears when there is a difference in the lattice parameters between different metal or alloy phases, which introduces compressive or tensile strain in the crystal lattice. In most cases, these effects appear simultaneously.[45, 46] In addition to the higher catalytic activity, the dealloying of Ni could lead to the higher catalytic activity toward the ORR after several thousand cycles, which provided a possible new approach to improve the catalytic activity and durability of the Pt catalyst series.

Based on the two-step preparation method of Pt-nanoparticle-supported carbon electrocatalysts in ionic liquid, I attempted to develop a one-pot pyrolysis method to produce sophisticated ORR electrocatalysts using IL solutions consisting of *N*,*N*,*N*-trimethyl-*N*-propylammonium bis(trifluoromethanesulfonyl)amide ($[N_{1,1,1,3}][Tf_2N]$), untreated MWCNTs, and thermally reducible Pt and/or Ni precursors. The electrocatalytic performances of the

resultant Pt and PtNi alloy nanoparticle-supported multi-walled carbon nanotubes (Pt/MWCNTs and PtNi/MWCNTs) were examined by electroanalytical measurements in a 0.1 M $HClO_4$ aqueous solution and the effect of the addition of Ni atoms to the Pt nanoparticles on the catalytic performance was investigated so as to gain further insight about how to design better electrocatalysts.

1-2. Experimental section

1-2-1. Synthesis of $Ni[Tf_2N]_2$

Nickel bis(trifluoromethanesulfonyl)amide ($Ni[Tf_2N]_2$) was synthesized by referring to previous papers.[47, 48] Bis(trifluoromethanesulfonyl)imide (Morita Chemical Industry Co., Ltd., 1.65 g) was dissolved in 36 mL of pure water. After bubbling N_2 for 30 min, $Ni(OH)_2$ (Waco Pure Chemical Industry Co. Ltd., 0.27 g) was added into the aqueous solution, and the mixture was heated for 2 h at 343 K. The resulting yellow precipitate was collected and dried at 453 K for 4 h to obtain anhydrous $Ni[Tf_2N]_2$. The final product was green.

1-2-2. Preparation of Pt/MWCNTs and PtNi/MWCNTs

PtNi/MWCNTs-dispersed IL was prepared by stirring the $[N_{1,1,1,3}][Tf_2N]$ (Kanto Chemical Co., Inc., 2 mL) containing 2.5 mg of untreated MWCNTs overnight at room temperature. Pt and PtNi alloy nanoparticle-supported-MWCNTs were fabricated by agitating the MWCNTs-dispersed IL with platinum(II) acetylacetonate ($Pt(acac)_2$, Mitsuwa Chemicals Co., Ltd.), and

$Ni[Tf_2N]_2$ or nickel(II) acetylacetonate ($Ni(acac)_2$, Sigma-Aldrich Co., LLC.) at 573 K for 4 h under N_2 atmosphere. The heating times for the Pt/MWCNTs and PtNi/MWCNTs were 6 hours and 4 hours, respectively, because their catalytic properties were worse if the heating time shortened. The crude materials obtained were washed with acetonitrile several times and dried under vacuum to obtain Pt/MWCNTs and PtNi/MWCNTs. The preparation conditions for Pt/MWCNTs (specimen **1**) and PtNi/MWCNTs (specimens **2**-**4**) are summarized in Table 1-1. A commercially available Pt nanoparticle catalyst (specimen **5**, TEC10V30E, Tanaka Kikinzoku Kogyo) was used as a reference.

1-2-3. Characterization of precursors, Pt/MWCNTs and PtNi/MWCNTs

Thermogravimetric (TG) analysis of the precursors used, namely $Pt(acac)_2$, $Ni[Tf_2N]_2$ and $Ni(acac)_2$, were conducted using a Bruker TG-DTA2000SA thermal analysis system under dry N_2 flow (100 mL min^{-1}) from room temperature to 873 K at 10 K min^{-1}. The temperature at which a 3 wt% loss from the original weight occurred was defined as the thermal decomposition temperature of the precursors. The X-ray diffraction (XRD) patterns of the Pt/MWCNTs and PtNi/MWCNTs were examined using a Rigaku Ultima IV using a Cu Kα radiation source. The diffraction patterns were taken from 20° to 80° at a scanning rate of 1° min^{-1}. The morphology of Pt/MWCNTs and PtNi/MWCNTs was observed by a Hitachi H-7650 transmission electron microscope (TEM). Elemental analysis of the specimens was performed with an EDAX Genesis-XM2 energy dispersive X-ray spectrometry (EDS) mounted on the

TEM. EDS mapping and high-angle annular dark-field (HAADF) images of the PtNi/MWCNTs were obtained using a JEOL ARM-200F TEM system. All the TEM sample grids were prepared by the procedure described in our previous papers.[31, 35-37] Surface analysis of the specimens was conducted by X-ray photoelectron spectroscopy (XPS) using a KRATOS AXIS-ULYRA DLD. The atomic percentages (at%) of Pt and Ni in the PtNi alloy nanoparticles on the MWCNTs were determined using a Shimadzu ICPS-7510 inductively coupled plasma atomic emission spectrometer (ICP-AES) after the dissolution of the alloy nanoparticles in aqua regia.

1-2-4. Electrochemical measurements

The electrochemical behaviors of the Pt/MWCNTs and PtNi/MWCNTs were investigated using a Hokuto Denko HZ-7000 electrochemical measurement system and a Pine Instruments Co. AFMSRCE rotating electrode speed controller. The electrochemical measurements were conducted using a three-electrode cell at room temperature (ca. 298 K) with a glassy carbon (GC) rotating disk electrode (RDE; 0.196 cm^2). A Pt mesh, an Ag/AgCl/KCl saturated aqueous solution electrode with a double-junction, and a 0.1 M $HClO_4$ aqueous solution were used as the counter and reference electrodes, and the electrolyte, respectively. The aqueous solution was thoroughly deaerated with N_2 gas or saturated with O_2 gas before each experiment. The resulting Pt/MWCNTs or PtNi/MWCNTs were dispersed in *i*-propanol solution with a weight concentration of 1.48 g L^{-1}. The black ink (10 μL) was spread onto the surface of the GC RDE,

and then dried naturally. Furthermore, 10 μL of Nafion®-dispersed *i*-propanol (0.1 wt%) was applied onto the electrode to fix the Pt/MWCNTs or PtNi/MWCNTs with a thin Nafion® layer. In order to remove the ionic liquid adsorbed onto the Pt nanoparticles, the Pt/MWCNTs and PtNi/MWCNTs working electrodes were electrochemically cleaned by 40-100 cycles of potential sweeps between 0.05 and 1.20 V, at a scan rate of 50 mV s^{-1}, and under a N_2 atmosphere, until the steady-state voltammograms were obtained. After the cleaning process, voltammetric experiments were conducted at 10 mV s^{-1} between 0.05 V and 1.20 V (*vs.* RHE), at room temperature, to estimate the electrochemical surface area (ECSA), as will be described below.

The ECSA of Pt and PtNi alloy nanoparticles was estimated from the hydrogen atom adsorption or desorption coulombic charge in the cyclic voltammogram measured under a N_2 atmosphere after subtracting the double layer charge current. The value of the ECSA was obtained by the following equation

$$\mathrm{ECSA}\ \ (\mathrm{m^2}\ \ \mathrm{g^{-1}}) = \frac{Q_{\mathrm{H}}\ \ (\mu\mathrm{C}) \times 10^2}{210\ \ (\mu\mathrm{C}\ \ \mathrm{cm^{-2}}) \times M_{\mathrm{Pt}}\ \ (\mu\mathrm{g})} \qquad (1)$$

where Q_H (μC) is the charge of hydrogen atom adsorption/desorption.[49] An average value for the charge associated with a hydrogen adsorption/desorption monolayer formed on smooth polycrystalline Pt is 210 μC cm^{-2}. M_{Pt} (μg) is the Pt weight on the GC working electrode. The

ORR performances of specimens were examined by rotating disk electrode-linear sweep voltammetry (RDE-LSV) in the anodic direction, with a sweep rate of 10 mV s^{-1}, and under five different rotating speeds (200, 400, 800, 1200, and 1600 rpm) in an O_2 atmosphere. The voltammograms obtained were characterized by the Koutecký-Levich equation as follows:

$$\frac{1}{I} = \frac{1}{I_k} + \frac{1}{B\omega^{1/2}} \qquad (2)$$

$$B \ \ (\mathrm{A\ \ s^{1/2}}) = 0.62nFAC^{*}D^{2/3}\nu^{-1/6}\omega^{1/2}$$

where I is the experimentally measured current (A) at 0.85 V, I_k is the kinetic current (A), ω is the electrode rotation rate (s^{-1}), n is the electron-transfer number, F is the Faraday constant (96485 C mol^{-1}), A is the electrode surface area (cm^2), C^* is the O_2 concentration in the electrolyte (mol cm^{-3}), D is the diffusion coefficient of O_2 in the electrolyte (cm^2 s^{-1}), and ν is the kinematic viscosity of the electrolyte (cm^2 s^{-1}). The I_k value was then estimated from the intercept of the Koutecký-Levich plot (I^{-1} *vs.* $\omega^{-1/2}$) and was normalized to the Pt loading of each specimen to obtain mass activities.

The durability of the electrocatalysts was examined by a standard degradation test recommended by the Fuel Cell Commercialization Conference of Japan.[46, 50] This test overloads the cathode for a proton-exchange membrane (PEM) fuel cell system by potential

sweeps between 1.00 and 1.50 V (*vs.* RHE) at 500 mV s^{-1}, causing carbon corrosion with ease. In other words, I can conduct a quick durability evaluation of the cathode catalyst by electrochemical means. In order to obtain more insight into the deterioration behavior, the catalytic activity retention rates for the ECSA and for the mass activities were estimated by the following equations:

Catalytic activity retention rate for ECSA (%)

$$= \frac{\text{ECSA estimated at each cycle } (\text{m}^2\ \text{g}_{\text{Pt}}{}^{-1})}{\text{initial ECSA } (\text{m}^2\ \text{g}_{\text{Pt}}{}^{-1})} \times 100 \qquad (3)$$

Catalytic activity retention rate for mass activity (%)

$$= \frac{\text{mass activity estimated at each cycle } (\text{A}\ \text{g}_{\text{Pt}}{}^{-1})}{\text{initial mass acitvity } (\text{A}\ \text{g}_{\text{Pt}}{}^{-1})} \times 100 \qquad (4)$$

1-3. Results and discussion

1-3-1. Characterization of obtained Pt/MWCNTs and PtNi/MWCNTs

It is essential for the synthesis of Pt/MWCNTs and PtNi/MWCNTs by a one-pot pyrolysis method to find a reasonable reaction temperature. The thermal behavior of metal precursors used in the one-pot method was examined. Figure 1-1 shows the TG curves of the three types of metal precursors used in this study, $Pt(acac)_2$, $Ni[Tf_2N]_2$ and $Ni(acac)_2$, as well as of the

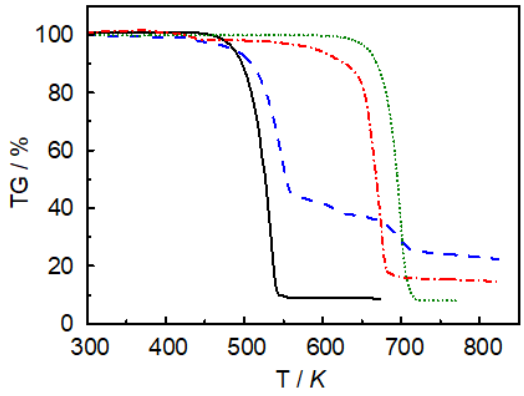

Fig. 1-1 TG measurement results of (—) $Pt(acac)_2$, (- · - · -) $Ni[Tf_2N]_2$, (- - -) $Ni(acac)_2$ and (· · ·) $[N_{1,1,1,3}][Tf_2N]$. The measurements were conducted at 10 K min^{-1}.

reaction medium, $[N_{1,1,1,3}][Tf_2N]$. Thermal decomposition behavior of the $Pt(acac)_2$ and

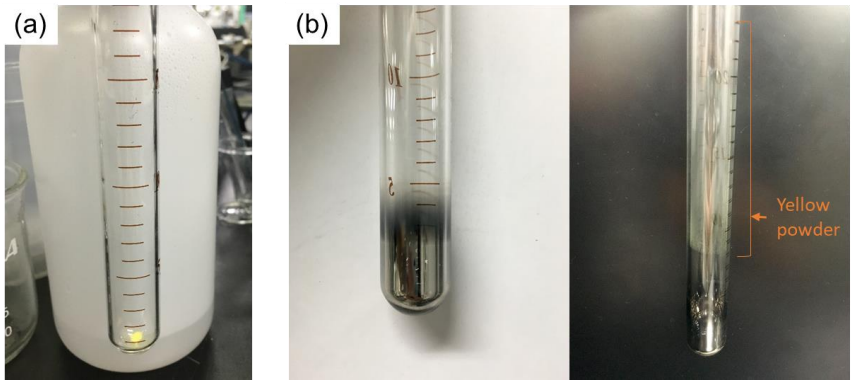

Fig. 1-2 Photographs of a test tube containing $Pt(acac)_2$ (a) before and (b) after heating. The test tube was heated at 10 K min^{-1} from room temperature to 473 K.

$Ni(acac)_2$ is basically the same as reported data.[51, 52] The order of their decomposition temperatures at the 3 wt% loss point of the TG curve is as follows: $[N_{1,1,1,3}][Tf_2N]$ (648.1 K), $Ni[Tf_2N]_2$ (552.0 K), $Pt(acac)_2$ (480.1 K), and $Ni(acac)_2$ (460.4 K). This result shows that this IL is a suitable reaction medium for preparing Pt/MWCNTs and PtNi alloy/MWCNTs by our approach. The decomposition temperature of $Ni[Tf_2N]_2$ is much higher than that of $Pt(acac)_2$ and $Ni(acac)_2$. Moreover, I confirmed that the pyrolytic reaction at 573 K is complete within 2 hours. As to the Ni precursors, their residual weights are almost the same as the Ni metal weight

estimated for the original one. However, this is not the case with $Pt(acac)_2$. Its residual weight is significantly lower than that expected from the estimation because of the sublimation of $Pt(acac)_2$. Figure 1-2 shows a photograph of the yellow $Pt(acac)_2$ powder in a test tube before and after the heating process from room temperature to 473 K. Sublimated $Pt(acac)_2$ appears on the inner wall of the tube, and a mirror-like deposit that is probably a Pt metal thin film is recognized at the bottom of the tube. Fortunately, this sublimation did not need to be considered in the present study because the dissolution of $Pt(acac)_2$ in the IL was found to completely suppress this behavior. Probably, $Pt(acac)_2$ was stabilized in the IL, thus making its sublimation temperature higher.

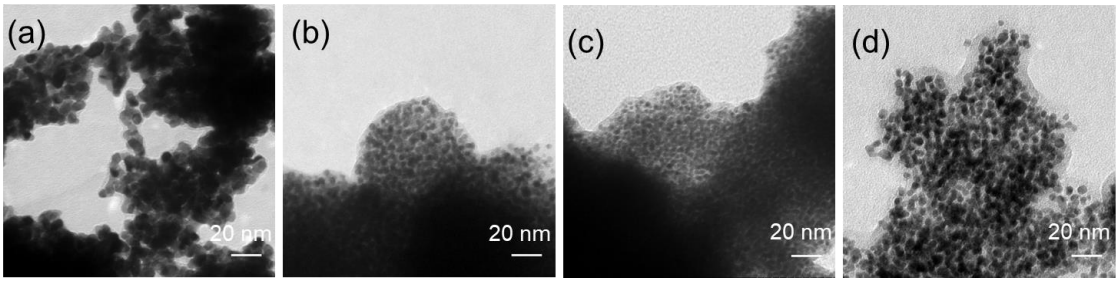

Fig. 1-3 TEM images of nanoparticles prepared at same condition as specimen (a) **1**, (b) **2**, (c) **3** and (d) **4** without MWCNT.

Prior to the fabrication of the Pt/MWCNTs and PtNi alloy/MWCNTs, I performed Pt and PtNi nanoparticle formation by pyrolysis of Pt and/or Ni precursors in $[N_{1,1,1,3}][Tf_2N]$ IL at 573 K. In the IL with only $Pt(acac)_2$, spherical Pt nanoparticles were obtained and the mean particle size was 6.9 nm (Figure 1-3). On the other hand, the nanoparticles prepared in the IL with both Pt and Ni precursors, showed mean sizes of ca. 3.0 to 5.0 nm. I revealed that the nanoparticle-monodispersed IL is readily produced by this pyrolytic approach, as is the case for Pt

magnetron sputtering onto ILs.[30-40] For reference, the detailed characterization data of the nanoparticles are summarized in Table 1-2.

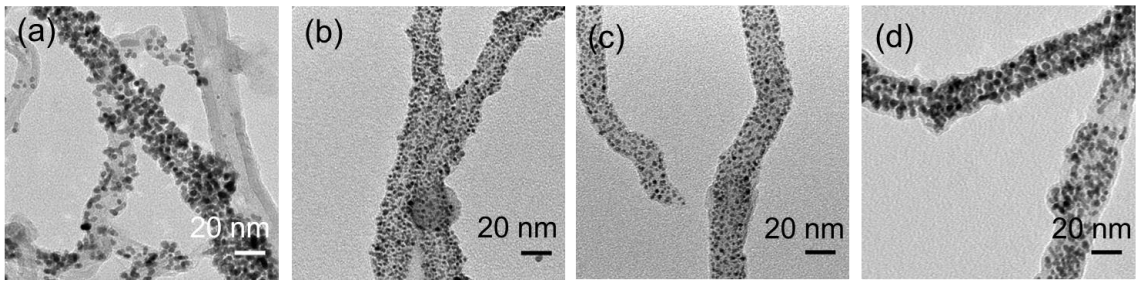

Fig. 1-4 TEM images of specimen **1**-**4** prepared by experimental conditions given in Table 1-1. The specimens are (a) **1**, (b) **2**, (c) **3** and (d) **4**.

Figure 1-4 shows the TEM images of specimens **1**-**4** prepared by the one-pot pyrolysis method under different conditions, given in Table 1-1. The deposited nanoparticles exhibit a spherical shape and are well dispersed onto the MWCNTs. If the acetylacetonate precursors, $Pt(acac)_2$ and $Ni(acac)_2$, are employed in this method, the mean particle sizes of the nanoparticles become larger compared to the case where $Ni[Tf_2N]_2$ is employed. This is probably due to the lower thermal decomposition temperature of the acetylacetonate precursors. The same tendency is recognized even when a combination of $Pt(acac)_2$ and $Ni[Tf_2N]_2$ is used for the preparation, i.e., the particle size increases at higher $Pt(acac)_2$ concentrations (specimen **2** and **3**). These results are essentially identical to those obtained from the IL without MWCNTs.

The Pt and Ni loading amounts on MWCNTs of specimens **1**-**4**, which was determined by ICP-AES, are given in Table 1-1 along with the data of the commercial catalyst, specimen **5**. Specimen **2**, which was prepared from the IL containing the highest $Pt(acac)_2$ concentration, shows the highest Pt loading amount (37.5 wt%). The Pt loading amounts of the other three

specimens are 22.4~28.2 wt%. The values are close to that of specimen **5**. The Pt and Ni contents of the nanoparticles deposited on the specimens are also shown in Table 1-1. The highest Ni composition (42.7 at%) in the nanoparticles is obtained in specimen **4**. However, all the Ni compositions in specimens **1**-**4** were less than the values expected from the concentration ratios of Pt precursor to Ni precursor. A possible reason is that even if more Ni metal is deposited, it could be dissolved by a substitution reaction between the Ni metal and the Pt(II) ion due to the large difference in their standard electrode potential (1.445 V in aqueous solution).[53] In addition to this, the alloy compositions in specimens **3** and **4** are different, even though these specimens were prepared with the same Pt and Ni precursor ratio. This is probably provoked by the difference in thermal stability of the Ni precursors used. This finding suggests that the Pt and Ni compositions in the specimens can be controlled to a certain degree by changing the metal precursor species.

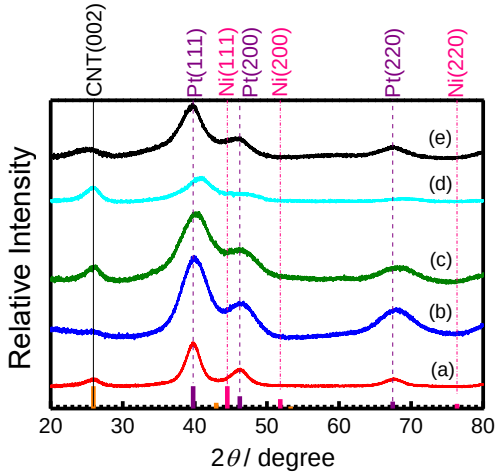

Fig. 1-5 X-ray diffraction patterns of specimen (a) **1**, (b) **2**, (c) **3**, (d) **4** and (e) TEC10V30E. The reflections from Pt metal (ICDD No.00-04-0802), Ni metal (ICDD No.00-04-0850) and carbon nanotube (ICDD No.00-058-1638) are denoted at the bottom of the figure.

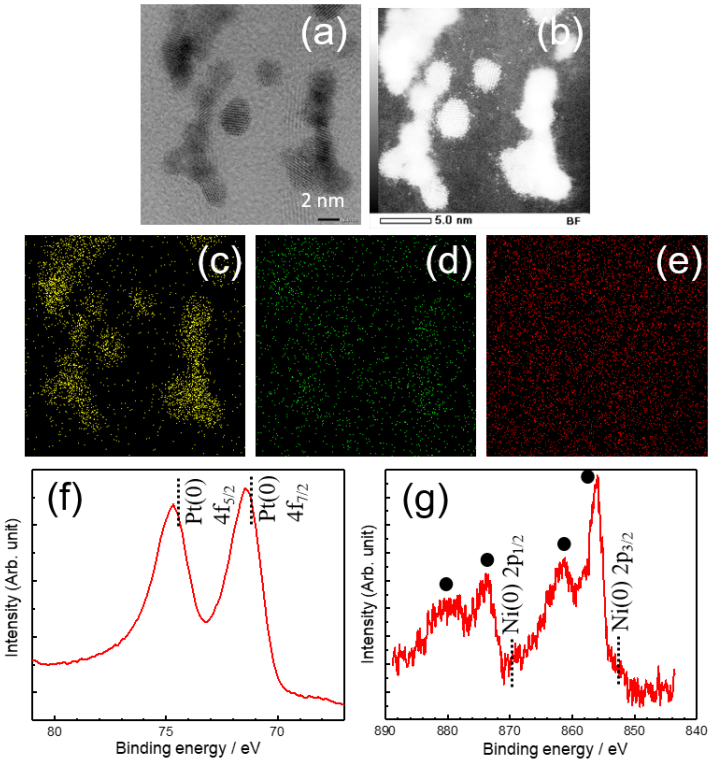

Figure 1-6. (a) High resolution TEM image, (b) HAADF-STEM image, (c-e) EDS mappings, and (f, g) XPS spectra of specimen **3**. The elements are (c, f) Pt, (d, g) Ni, and (e) C. The filled circles, ●, shown in (g) are the XPS spectra related to Ni_2O_3.

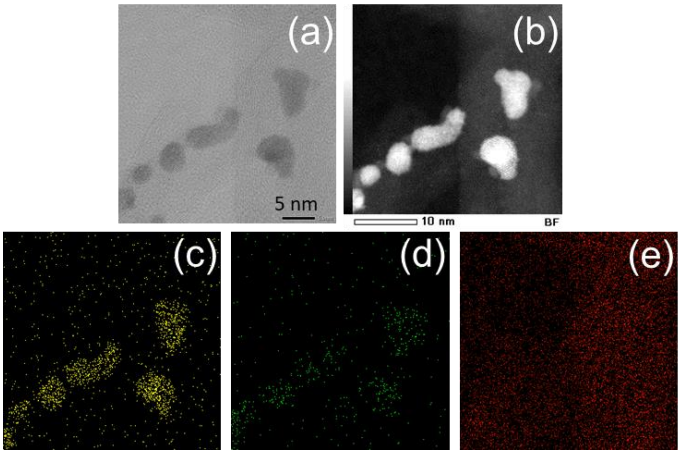

Fig. 1-7 (a) High resolution TEM image, (b) HAADF-STEM image and (c-e) EDX mappings of specimen **4**. The elements are (c) Pt, (d) Ni and (e) C.

The XRD patterns of specimens **1-5** are indicated in Figure 1-5. As to specimen **1**, the diffraction pattern derives from the carbon nanotubes (ICDD No.00-058-1638) and the pure Pt metal (ICDD No.00-04-0802). Moreover, specimens **2-4** show similar diffraction patterns, but

the peaks for the Pt metal are slightly shifted to a higher angle. The observed shift in the Pt reflections to larger 2θ values is due to the increase in the Ni content of the nanoparticles as smaller Ni atoms are substituted for Pt atoms in the lattice.[54] There is no diffraction related to the Ni metal. To further investigate the compositional distributions of Pt and Ni in nanoparticles on the specimens, high-resolution TEM, HAADF-scanning transmission electron microscopy (STEM), and EDS mapping images were obtained. Those for specimens **3** and **4** are shown in Figure 1-6 and Figure 1-7, respectively. The high-resolution TEM images show that crystalline PtNi alloy nanoparticles are deposited on the MWCNTs. The HAADF-STEM and EDS mapping images indicate that Pt and Ni are present in the same region and Ni atoms are distributed uniformly in the Pt nanoparticles. The results of EDS quantitative analysis are summarized in Table 1-2. The composition ratio of Pt and Ni in the specimens **1**-**4** was nearly identical to that of the nanoparticles yielded without MWCNTs. XPS spectra of specimen **3** also suggest the PtNi alloy formation, while the spectra for Ni metal is weak compared to that for Ni_2O_3 and that for Pt metal slightly shifts to the higher binding energy, which is commonly observed when Pt alloys with Ni, Co, and Fe are formed (Figure 1-6).[54] Through the various analyses of the specimens performed in this study, I reached the conclusion that the nanoparticles on specimens **2**-**4** are PtNi alloy nanoparticles and the one-pot pyrolysis method, which would be suitable for the mass production process, can effectively produce Pt/MWCNTs and PtNi/MWCNTs

Table 1-1 Summary of specimen **1-4** prepared in this chapter

Specimen	Metal salt concentration / mM			Agitation time / h	Mean particle size[a] / nm	Loading amount / wt%		Composition of nanoparticle / at%	
	$Pt(acac)_2$	$Ni[Tf_2N]_2$	$Ni(acac)_2$			Pt	Ni	Pt	Ni
1	5		-	6	2.9 (0.6)[a]	28.2	-	100.0	-
2	15	5	-	4	1.9 (0.5)[a]	37.5	2.2	83.8	16.2
3	5	5	-	4	1.6 (0.5)[a]	22.4	3.4	66.4	33.6
4	5	-	5	4	3.3 (0.8)[a]	27.0	6.0	57.3	42.7
TEC10V30E	-	-	-	-	2.6 (0.7)[a]	23.7	-	-	-

[a] The values in parentheses are standard deviations.

Table 1-2. Summary of Pt and PtNi alloy nanoparticles obtained by different pyrolytic conditions

Metal precursor concentration / mM			Agitation time / h	Mean particle size[a] / nm	Composition of nanoparticle[c] / at%			
					Without MWCNTs		With MWCNTs[c]	
$Pt(acac)_2$	$Ni[Tf_2N]_2$	$Ni(acac)_2$			Pt	Ni	Pt	Ni
5		-	6	6.9 (1.2)[b]	100	-	100	-
15	5	-	4	4.0 (0.7)[b]	91	9	89	11
5	5	-	4	3.0 (0.5)[b]	73	27	72	28
5	-	5	4	4.9 (0.9)[b]	38	62	42	58

[a] The composition of the resulting nanoparticles was calculated from EDS measurement.

[b] The values in parentheses are standard deviations.

[c] These values show the composition of the specimens **1-4** determined from EDS measurement.

1-3-2. Electrocatalytic activity and durability of Pt/MWCNTs and PtNi/MWCNTs

Figure 1-8 shows cyclic voltammograms taken of specimens **1**-**5** at a glassy carbon electrode, in a N_2-saturated 0.1 M $HClO_4$ aqueous solution, before and after 15000 potential cycle tests. Typical redox waves related to the hydrogen adsorption/desorption and oxygen reactions appear at the potentials ranging from 0.10 to 0.35 V and from 0.60 to 1.00 (*vs*. RHE),

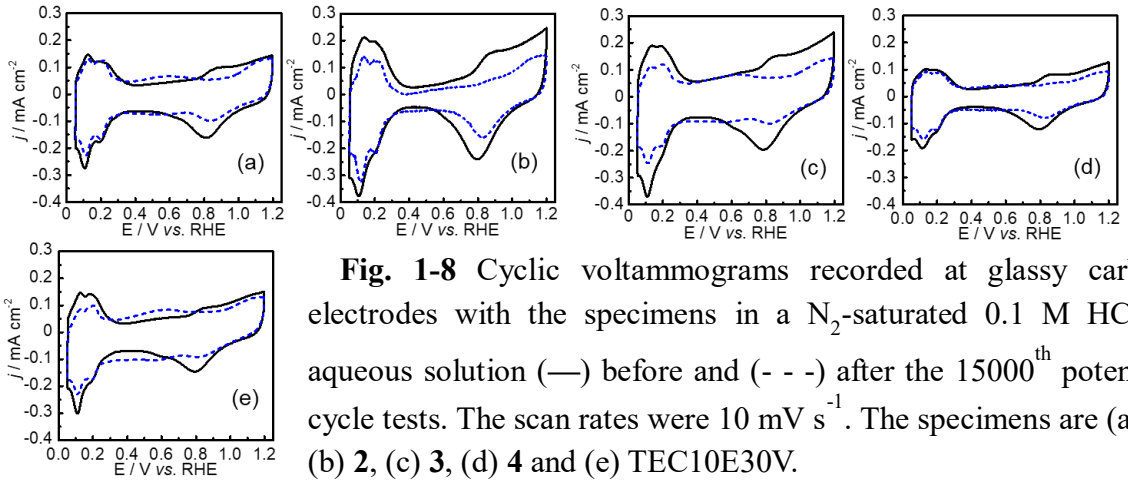

Fig. 1-8 Cyclic voltammograms recorded at glassy carbon electrodes with the specimens in a N_2-saturated 0.1 M $HClO_4$ aqueous solution (—) before and (- - -) after the 15000th potential cycle tests. The scan rates were 10 mV s^{-1}. The specimens are (a) **1**, (b) **2**, (c) **3**, (d) **4** and (e) TEC10E30V.

respectively, in all the voltammograms. After the cycle test, these redox waves become small, and a couple of new reduction and oxidation waves appear around ca. 0.60 V. The appearance of new redox waves implies that carbon corrosion proceeds during the potential cycle test via oxidation of the functional groups on the carbon support to CO_2 and CO, and is enhanced in the presence of Pt nanoparticles.[55, 56] At the electrode with specimen **5** that uses carbon black as a support material, it is more apparent because carbon black is more susceptible to damage than MWCNTs. The voltammograms for specimens **2** and **3** show a much larger area at the potential range related to hydrogen atom adsorption/desorption, since their mean particle sizes

are smaller than those of other specimens (Table 1-1). On the other hand, specimen **4**, which consists of the largest nanoparticles, shows the smallest area. As shown in Table 1-3, the initial ECSA of the specimens used in this investigation became larger in the order of: specimen **4** (30.1 $m^2 g^{-1}$), specimen **1** (39.7 $m^2 g^{-1}$), specimen **5** (40.4 $m^2 g^{-1}$), specimen **2** (56.6 $m^2 g^{-1}$), specimen **3** (58.5 $m^2 g^{-1}$).

The variation in the specimen ECSA during the catalyst durability test is represented in

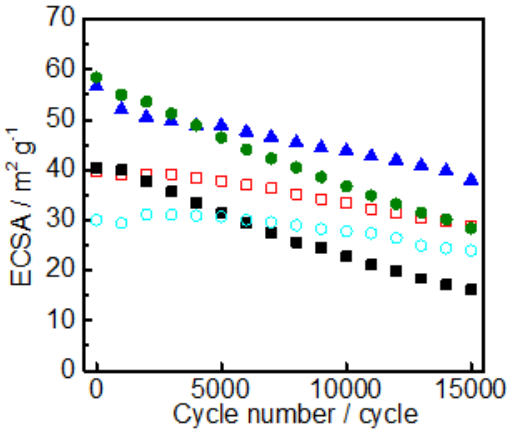

Fig. 1-9 Variation in ECSA estimated from cyclic voltammograms as a function of cycle number. The specimens are (□) **1**, (▲) **2**, (●) **3**, (○) **4** and (■) TEC10V30E.

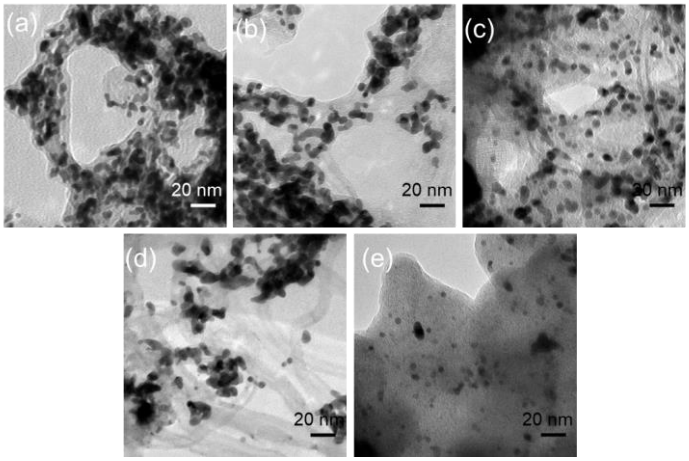

Fig. 1-10 TEM images of (a-d) specimen **1-4** and (e) TEC10V30E after 15000 cycle test. The specimens are (a) **1**, (b) **2**, (c) **3**, (d) **4**, (e) TEC10V30E.

Figure 1-9. The ECSA for all specimens tends to decrease with the cycle number. The retention rate for specimen **5** after 15000 cycles is only 40 %, but the other four specimens **1**-**4** show a better retention rate (Table 1-3). The main reason for the higher durability is the chemically inert MWCNT carbon support used for the preparation of specimens **1**-**4**. Another possible reason that should also be considered is that the thin IL layer, which exists between the Pt nanoparticle and the carbon support, prevents corrosion.[38-41] Amongst specimens **1**-**4**, specimen **4** shows a very high retention rate close to 85 %, while specimen **3** remains at ca. 50 %. Given the increase in the particle size after the durability test, especially for specimen **2** (Figure 1-10), the difference in the retention rate among specimens **1**-**4** would be dependent on the degree of nanoparticle aggregation.

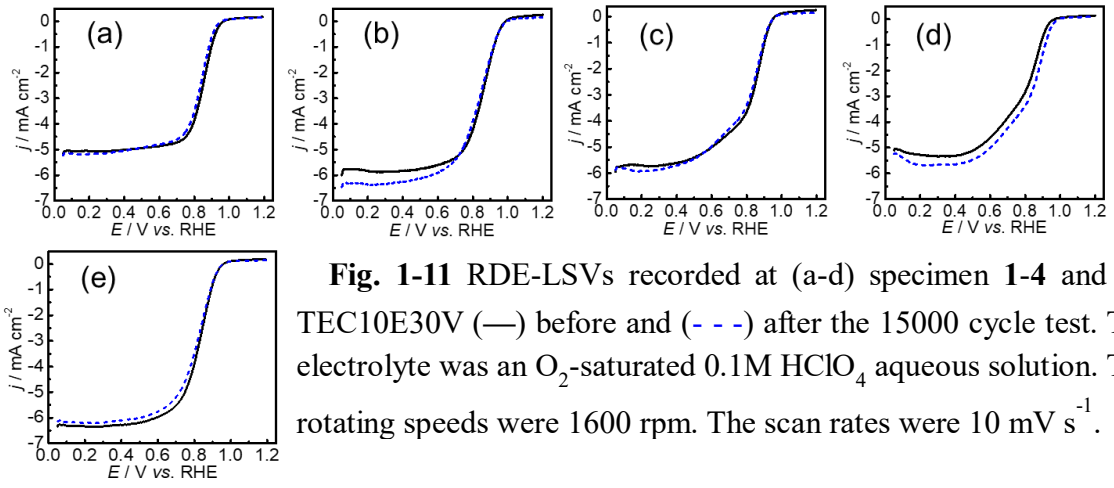

Fig. 1-11 RDE-LSVs recorded at (a-d) specimen **1**-**4** and (e) TEC10E30V (—) before and (- - -) after the 15000 cycle test. The electrolyte was an O_2-saturated 0.1M $HClO_4$ aqueous solution. The rotating speeds were 1600 rpm. The scan rates were 10 mV s^{-1}.

Since the mass activity for the ORR is the most important factor for evaluating electrocatalysts, it was also examined for all the specimens. Figure 1-11 shows the RDE-LSVs taken at glassy carbon rotating electrodes with specimens **1**-**5**, in an O_2-saturated 0.1 M $HClO_4$

aqueous solution, before and after 15000 potential cycle tests. Before the durability test, all the electrodes demonstrate an increase in current flow due to O_2 reduction at more negative potentials than ca. 1.05 ~ 1.10 V, as observed for commonly used electrocatalysts for the ORR. The current flows shift slightly to a negative potential after the 15000-cycle test, except for

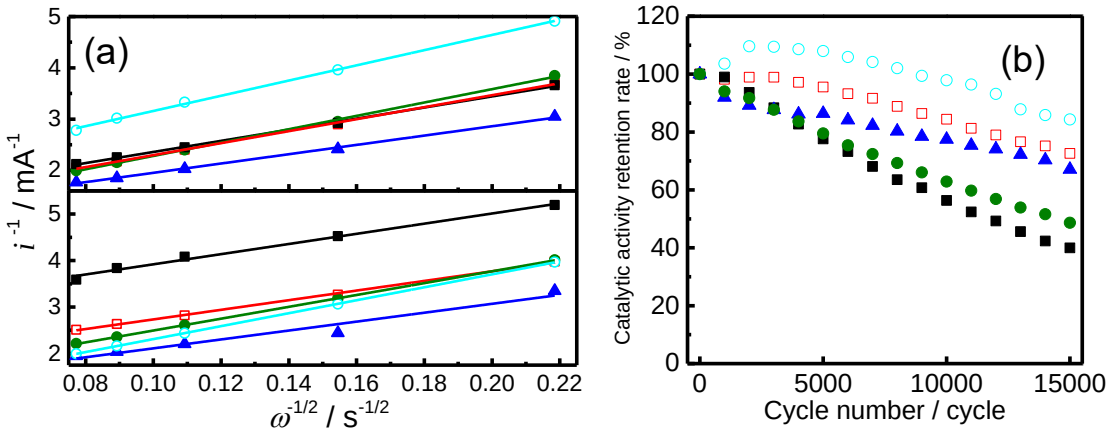

Fig. 1-12 Koutecký-Levich plots (a) before and (b) after durability tests. The potential for constructing the plots was 0.85 V. (c) Variation in surface retention rate estimated from the Koutecký-Levich plots as a function of cycle number. The specimens are (□) **1**, (▲) **2**, (●) **3**, (○) **4** and (■) TEC10V30E.

those of specimen **4**, which interestingly shows a different electrode behavior. In order to gain further insights into these catalytic behaviors, Koutecký-Levich plots at 0.85 V were constructed using RDE-LSVs obtained at different rotating speeds of 200 ~ 1600 rpm (Figure 1-12a). The mass activity data calculated from the Koutecký-Levich plots before and after the durability tests are summarized in Table 1-3 and Figure 1-12b. The initial mass activity of specimen **1** (212.3 A g^{-1}) is close to that of specimen **5** (224.3 A g^{-1}). This seems to be a reasonable result, considering that these two catalysts have Pt nanoparticles of similar size and that the nanoparticles are uniformly dispersed on the carbon supports. With regards to the PtNi

alloy supported electrocatalysts, specimens **2**-**4**, their mass activity behaviors are entirely different; specimen **2** (172.5 A g^{-1}) and **4** (150.2 A g^{-1}) show lower mass activity, but specimen **3** (307.9 A g^{-1}) has the highest mass activity. Note that specimens **2** and **3** have similar sized PtNi alloy nanoparticles on MWCNTs. These results imply that the particle size, as well as the

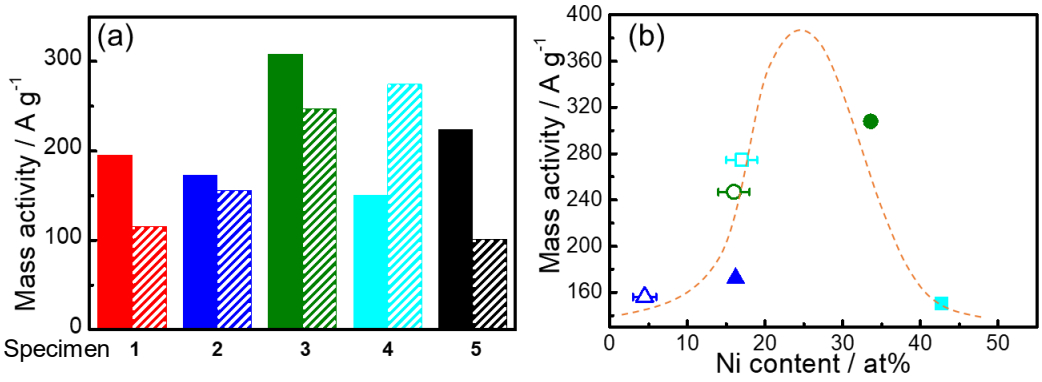

Fig. 1-13 (a) Comparison of mass activities of five specimens used in this research (filled bar) before and (diagonal bar) after 15000 cycle test. (b) Mass activities of PtNi/MWCNTs at different Ni contents. (▲, △) Specimen **2**, (●, ○) Specimen **3** and (■, □) Specimen **4**. (▲, ●, ■) before and (△, ○, □) after the cycle test.

alloy composition of the PtNi nanoparticle, are critical factors for increasing the mass activity. In contrast, the mass activities after the durability tests drastically change. Despite the similar initial activity, the mass activity of specimen **5** (101.2 A g^{-1}) goes below that of specimen **1** (141.0 A g^{-1}), probably because of a lower ECSA (16.1 m^2 g^{-1}). All the retention rates on the mass activity for the specimens prepared by the one-pot pyrolytic method surpass that for specimen **5** (45 %). The values become higher in the order of: specimen **1** (66 %), specimen **3** (80 %), specimen **2** (91 %), and specimen **4** (183 %) (Figure 1-13a). A major reason for this observation is possibly their high ECSA retention rates. I also have to consider another factor since it is quite difficult to explain the increment of mass activity for specimen **4** after the test

on the basis of the reason above. In fact, it is known that the ligand and strain effects can influence the catalytic activity of Pt alloy.[12-14] Therefore, all the mass activity data obtained in this study is depicted in Figure 1-13b as a function of the Ni content in the nanoparticles. The Ni content in the PtNi alloy nanoparticles after the test was determined using EDS. Interestingly, the variation in the mass activity follows a bell-shaped curve, with a peak at 25 at% Ni. Rudi *et al.* have reported similar bell-shaped behavior for the ORR activity.[18] Several other studies, including computational chemistry predictions, seem to support their idea.[42, 57]. The fact that the catalytically most active surface for the ORR is a segregated $Pt_3Ni(111)$ skin Pt single crystal facet[18, 58] implies that 25 at% is the perfect Ni content for achieving a very active facet. It is interesting to note that the mass activity behavior of the resulting PtNi/MWCNTs produced in this study can be explained using the bell-shaped curve. First, the anomalous mass activity behavior of specimen **4** before and after the durability test is considered to be caused by the excess Ni content (42.7 at%) in the PtNi alloy at the initial state and Ni leaching from PtNi alloy nanoparticles during the test. Similarly, the mass activity behavior for specimens **2** and **3** can also be elucidated by the bell-shaped curve. Specific activity of specimens **1**-**5** estimated from the ECSA and the mass activity are summarized in Table 1-3. Apparently specimens **2**-**4** indicate the higher retention rates of specific activity than Pt nanoparticle-supported electrocatalysts, specimens **1** and **5**. This result would be derived from the high retention rate of mass activity for specimens **2**-**4** described above.

Table 1-3 Summary of electrocatalytic properties for the specimens used in this chapter

Specimen	ECSA			Mass activity		
	Initial / $m^2\ g^{-1}$	After 15000 cycles / $m^2\ g^{-1}$	Retention rate / %	Initial / $A\ g^{-1}$	After 15000 cycles / $A\ g^{-1}$	Retention rate / %
1	39.7	28.8	73	212.3	141.0	66
2	56.6	38.0	67	172.5	156.2	91
3	58.5	28.4	49	307.9	247.0	80
4	30.1	24.0	84	150.2	274.6	183
TEC10V30E	40.4	16.1	40	224.3	101.2	45

1-4. Conclusions

Pt/MWCNTs and PtNi/MWCNTs electrocatalysts were successfully synthesized by a one-pot pyrolysis method with $[N_{1,1,1,3}][Tf_2N]$ IL containing untreated MWCNTs, and Pt and/or Ni precursors. The particle size of Pt and PtNi alloy nanoparticles on the Pt/MWCNTs and PtNi/MWCNTs was dependent on the precursor species. The use of thermally unstable acetylacetonate (acac)-based precursors made the particle size larger. All the prepared electrocatalysts showed better durability (the retention rate of mass activity: 66% ~ 183%) than that of a commercially available one (45%). Both the chemically inert nature of the MWCNTs and the existence of the thin IL layer between the Pt nanoparticles and the carbon support suppress carbon corrosion and lead to better durability of catalysts. The bell-shaped curve constructed in this article allows us to predict the mass activity of the PtNi/MWCNTs from the Ni content in the PtNi alloy nanoparticles. Since this one-pot process is suitable for mass production of valuable electrocatalysts for fuel cell applications, I believe that the one-pot process will greatly contribute to the further development of fuel cell technology.

Chapter 2

Investigation of PtNi Alloy Nanoparticle Formation in an Ionic Liquid Using a Staircase Heating Process

2-1. Introduction

It is not easy to vary the composition of the alloy while maintaining a desired particle size. To date, such Pt alloy nanoparticles have been prepared via commonly used methods, such as electrochemical deposition[26, 59-61] and colloidal synthesis,[62-65] wherein the latter is often preferred as it is an easier synthesis procedure.[66] In most cases, the synthesis is carried out through the following steps: *i*) seed growth, *ii*) deposition of the second metal on the seed, and *iii*) supporting of the prepared nanoparticles onto the carbon materials. By this multi-step growing method, Pt alloy nanoparticles can be designed stepwise. However, such a process is time-consuming, complicated, and unsuitable for a large-scale industrial process.

In the previous chapter, it was described that a simple and mass-producible one-pot pyrolysis method was established with an ionic liquid (IL one-pot process) for preparing Pt metal and PtNi alloy nanoparticle-supported multi-walled carbon nanotube composite (Pt/MWCNT and PtNi/MWCNT) electrocatalysts for ORR.[67] The PtNi/MWCNT prepared by the one-pot process in the IL, $[N_{1,1,1,3}][Tf_2N]$, with $Pt(acac)_2$, $Ni[Tf_2N]_2$, and MWCNT had a mass activity 1.4 times higher than that of a commercially available electrocatalyst. Such was not case when $Ni(acac)_2$ was used, thereby suggesting that the alloying process varies with the precursor species. In fact, other pyrolysis processes not using an IL as the reaction medium can roughly control the alloy composition by changing the preparation conditions, such as precursor species, precursor ratio, heating temperature, and reaction time.[68-71] Herein, to examine the PtNi alloy nanoparticle formation mechanism in an IL and to control the alloy composition, a staircase

heating process was employed for the one-pot pyrolysis process with an IL. The PtNi/MWCNTs collected throughout the heating process were characterized using TEM, XRD, ICP-AES, and electrochemical measurements. I determined the effects of the nickel precursor species and the heating conditions on the particle size and crystal structure of the PtNi nanoparticles as well as the catalytic performance of the PtNi/MWCNTs.

2-2. Experimental section

2-2-1. Preparation of PtNi/MWCNTs

The PtNi/MWCNT fabrication was conducted using a one-pot pyrolytic process under N_2 atmosphere. The reaction media were $Pt(acac)_2$ (Mitsuwa Chemicals Co., Ltd.), $Ni[Tf_2N]_2$ or $Ni(acac)_2$ (Sigma-Aldrich Co., LLC.), 2 mL of $[N_{1,1,1,3}][Tf_2N]$ IL (Kanto Chemical Co., Inc.), and 1.25 g L^{-1} of MWCNT (Sigma-Aldrich Co., LLC.). The IL mixtures were agitated at room-temperature overnight to uniformly disperse the precursors and MWCNTs. The concentration of the Pt and Ni precursors in the IL mixtures was 5 mmol L^{-1}. A staircase heating process was employed for the synthesis of PtNi/MWCNT. The heating conditions are graphically shown in Figure 2-1, and the samples taken from the IL mixture throughout the procedure are labeled A-L. The resulting PtNi/MWCNTs were washed with anhydrous acetonitrile multiple times and dried under vacuum overnight.

2-2-2. Characterization and electrochemical measurements

The morphology of the PtNi/MWCNTs was observed using a Hitachi H-7650 TEM; selected area electron diffraction (SAED) patterns were also obtained using the same instrument. Other characterization and electrochemical measurement of the PtNi/MWCNTs were carried out in the same method as in chapter 1.

2-3. Results and discussion

2-3-1. PtNi/MWCNTs formation mechanism

As shown in chapter 1 Fig. 1-1, TG measurements of the metal precursors and the IL, $[N_{1,1,1,3}][Tf_2N]$, indicated that the thermal decomposition of the nickel precursors gradually initiated prior to that of the Pt precursor. Moreover the $[N_{1,1,1,3}][Tf_2N]$ IL was a viable reaction medium for the IL-based one-pot process when the heating temperature was less than ca. 650 K. Based on these results, a staircase heating process with three temperature plateaus at 373 K, 473 K, and 573 K was employed to examine the nanoparticle formation mechanism during the

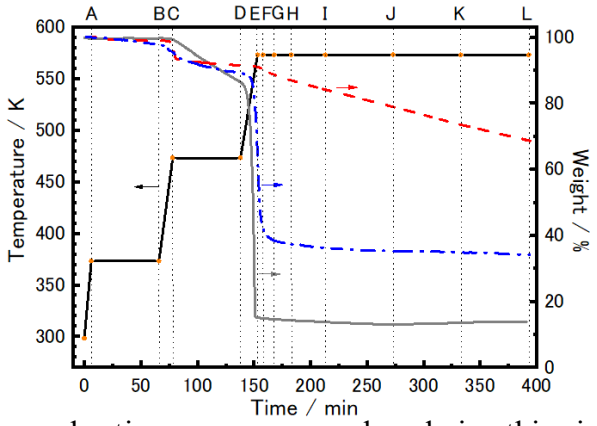

Figure 2-1. Staircase heating process employed in this investigation and TG measurement results of (—) $Pt(acac)_2$, (- - -) $Ni[Tf_2N]_2$, (- · - · -) and $Ni(acac)_2$ using the staircase heating process. Taking the samples from the IL mixtures with metal precursors and MWCNT was conduced at the point of A - L shown in a top axis.

one-pot process and was applied to TG measurements of the metal precursors (Figure 2-1). Slight weight losses for $Ni[Tf_2N]_2$ and $Ni(acac)_2$ were observed at the 373 K plateau. At the onset of the 473 K plateau, the weight losses became more clear and were nearly unchanged until the end of this plateau. As for $Ni(acac)_2$ and $Pt(acac)_2$, minimal corresponding weight loss resulting from metal deposition was observed after the onset of the plateau at 573 K. However, $Ni[Tf_2N]_2$ showed a constant weight loss throughout the heating plateau at 573 K.

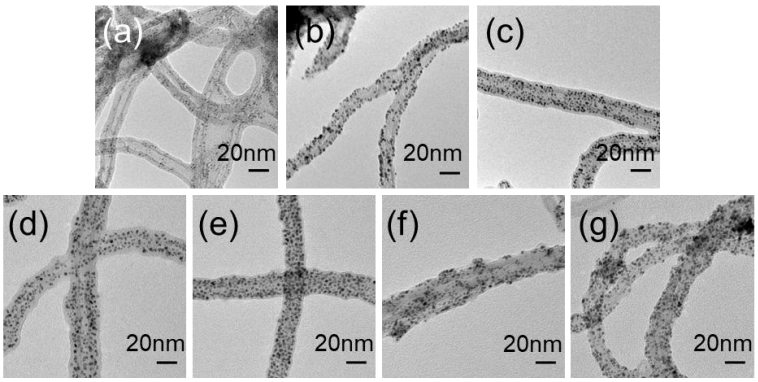

Figure 2-2. Typical TEM images of PtNi/MWCNTs prepared in the $[N_{1,1,1,3}][Tf_2N]$ with 5 mmol L^{-1} $Pt(acac)_2$, 5 mmol L^{-1} $Ni[Tf_2N]_2$, and 1.25 g L^{-1} MWCNT. Samplings of the IL mixture were conduced at the sampling points of (a) C, (b) D, (c) E, (d) I, (e) J, (f) K, and (g) L depicted in Figure 2-1.

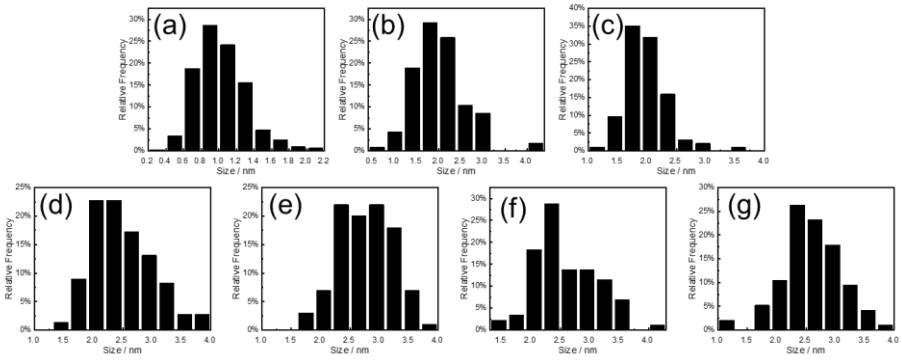

Figure 2-3. Particle size distribution histogram of nanoparticles of the specimen using $Ni[Tf_2N]_2$ determined from TEM image at the sampling points of (a) C, (b) D, (c) E, (d) I, (e) J, (f) K, and (g) L depicted in Figure 2-1.

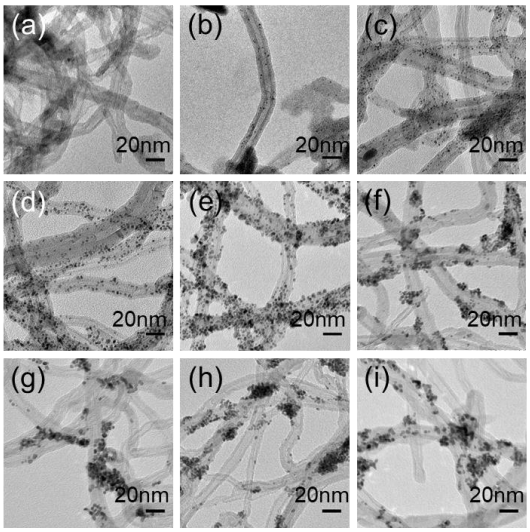

Figure 2-4. Typical TEM images of PtNi/MWCNTs prepared in the $[N_{1,1,1,3}][Tf_2N]$ with 5 mmol L^{-1} $Pt(acac)_2$, 5 mmol L^{-1} $Ni(acac)_2$, and 1.25 g L^{-1} MWCNT. Samplings of the IL mixture were conduced at the sampling points of (a) D, (b) E, (c) F, (d) G, (e) H, (f) I, (g) J, (h) K, and (i) L depicted in Figure 2-1.

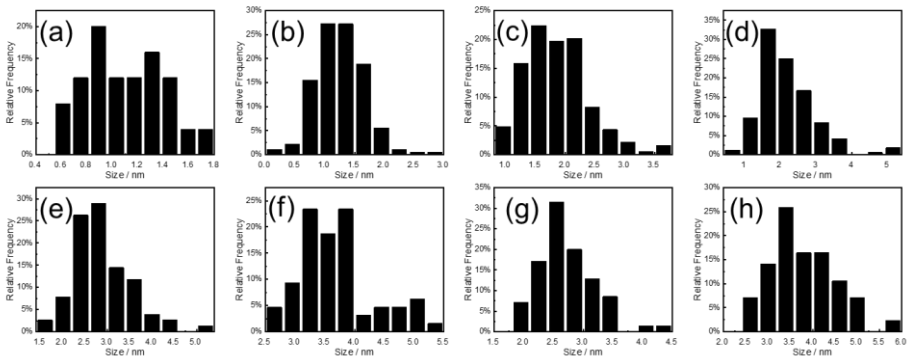

Figure 2-5. Particle size distribution histogram of nanoparticles of the specimen using $Ni(acac)_2$ determined from TEM image at the sampling points of (a) E, (b) F, (c) G, (d) H, (e) I, (f) J, (g) K, and (h) L depicted in Figure 2-1.

Further investigation was carried out using the staircase heating of the IL mixtures containing $Pt(acac)_2$, Ni precursors, and MWCNTs. Figure 2-2 shows TEM images of the specimens prepared in the $[N_{1,1,1,3}][Tf_2N]$ mixtures with $Ni[Tf_2N]_2$ as the Ni precursor. Mean particle sizes of the nanoparticles deposited on the MWCNTs are summarized in Table 2-1. Their particle size distributions estimated from the TEM images are exhibited in Figure 2-3. As may be expected from the thermal decomposition behavior of the metal precursors shown in Figure 2-1, no observable nanoparticles were produced at the heating temperature of 373 K, i.e., at sampling points A and B. However, once the temperature exceeded 473 K, tiny nanoparticles with a mean particle size of 1.0 nm deposited onto the MWCNTs (sampling point C). Prolonged heating time at 473 K resulted in larger nanoparticles (1.9 nm, sampling point D). Shortly after heating was raised to 573 K (sampling point E), the particle size increased to 2.4 nm. Throughout the prolonged heating at 573 K (sampling points I-L, Figure 2-2d-g), the mean particle size remained virtually constant with a standard deviation of ca. 0.5 nm, while the particle distribution on the MWCNTs broadened. When $Ni(acac)_2$ was used as the Ni precursor, it was difficult to observe the formation of nanoparticles on the MWCNTs from the samples taken during the 373 K and 473 K heating plateaus. However, the heat treatment at 573 K generated identifiable nanoparticles on the MWCNTs. Moreover, the mean particle size increased with increasing heating time. TEM images and mean particle sizes of the specimens

obtained at sampling points D–L are shown in Figure 2-4. Mean particle sizes and particle size distributions of the nanoparticles observed in Figure 2-4 are given in Table 2-2 and shown in Figure 2-5, respectively. The mean particle size increased with increasing heating time. At sampling point L, the particle size became 3.7 nm and was significantly larger than that of the nanoparticles obtained from the IL mixture containing $Ni[Tf_2N]$.

Tracking the change in the composition ratio of the nanoparticles can lead to interesting insights into the nanoparticle formation mechanism. The Ni contents of the nanoparticles on

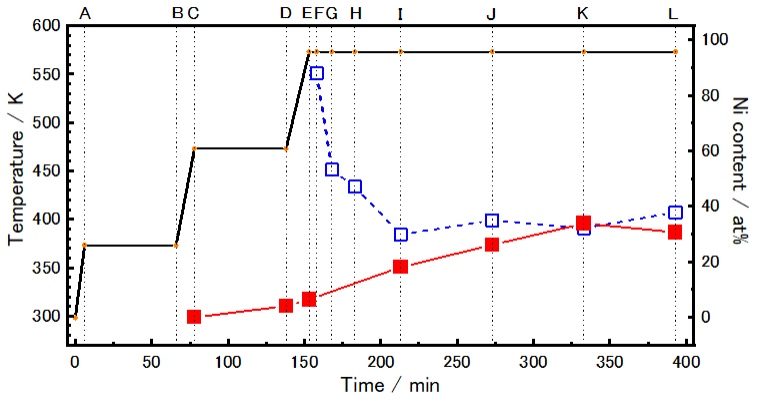

Figure 2-6. Ni contents in the nanoparticles deposited MWCNTs in the IL-MWCNTs mixtures with $Pt(acac)_2$ and (—■—) $Ni[Tf_2N]_2$ or (- -□- -) $Ni(acac)_2$. The Ni contents were determined by ICP-AES.

MWCNTs prepared in the IL mixtures under various heating conditions are shown in Figure 2-6. For the specimens obtained from the IL mixtures containing $Ni[Tf_2N]_2$, the Ni content of the nanoparticles was considerably low (up to 4 at%) until the onset of the heating plateau at 573 K, wherein Ni content gradually and linearly increased for the next 2 hours and finally remained at approximately 30 at%. The variation of the Ni content of the specimens produced in the IL mixtures containing $Ni(acac)_2$ was the opposite. That is, at the onset of the plateau at 573 K (sampling point F), the Ni content was approximately 90 at% but rapidly decreased to ca. 30 at% within 60 min. Interestingly, all the specimens obtained at sampling points I-L had similar Ni contents, ca. 34 ± 4 at%. Throughout the heating processes at 373 K and 473 K, most of the limited number of Ni metal nanoparticles produced were likely consumed by the

electrochemical substitution reaction between Ni(0) and Pt(II). I deduced that this reaction step hampered the formation of Ni metal nanoparticles at the said temperatures, and thus nucleation was more difficult in the IL mixture containing $Ni(acac)_2$. Because nucleation was difficult and the particle growth proceeded on the minimal nuclei, the resulting nanoparticles were larger, as summarized in Table 2-2.

Further information on the crystal structure of the nanoparticles deposited on MWCNTs was collected using XRD measurements. As shown in Figure 2-7a, all the Pt diffraction patterns of

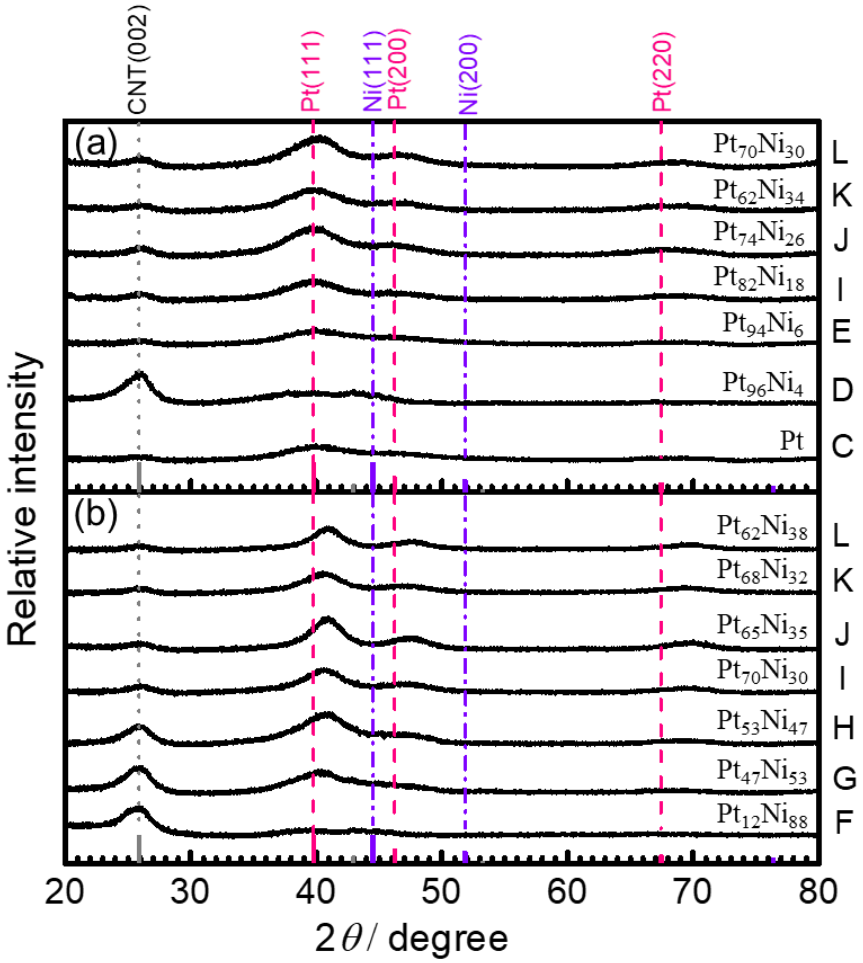

Figure 2-7. X-ray diffraction patterns of the PtNi/MWCNTs prepared with (a) $Ni[Tf_2N]_2$ and (b) $Ni(acac)_2$. The sampling points and the PtNi alloy nanoparticle compositions in the specimens are denoted on the graph.

the specimens prepared in the mixture containing $Ni[Tf_2N]_2$ appear similar, except for that of the sample obtained at point L. However, the Pt diffraction pattern of the sample taken at point L showed a slight shift to a higher angle, suggesting that PtNi alloy nanoparticles with a face-

centered cubic (fcc) solid solution phase were formed under the experimental conditions.[72, 73] Although the Ni content at point L was similar to that of the specimens taken at sampling points J and K, the XRD patterns of samples taken at points J and K did not show similar behavior to that of L. This may indicate Pt/Ni or Pt/patch-like Ni core-shell structure formation.[74, 75] For the IL mixture containing $Ni(acac)_2$, all the XRD patterns of the specimens notably shifted to a higher angle, except for that of the Ni-rich specimen at sampling point F, due to the formation of PtNi alloy nanoparticles with an fcc solid solution phase (Figure 2-7b). The results of the XRD measurements indicate that a PtNi alloy solid solution nanoparticle with an fcc crystal structure was eventually produced on the MWCNTs during the staircase heating process regardless of the Ni precursor used. However, the alloy formation mechanism itself depended on the Ni precursor species used. As indicated in Figure 2-8, SAED patterns of the specimens collected at sampling point L also corroborate the aforementioned conclusion.

Differences in the nanoparticle formation temperatures of Pt and Ni, T_{Pt} and T_{Ni}, respectively, estimated from Figure 2-6, seemed to cause the different PtNi alloy formation mechanisms

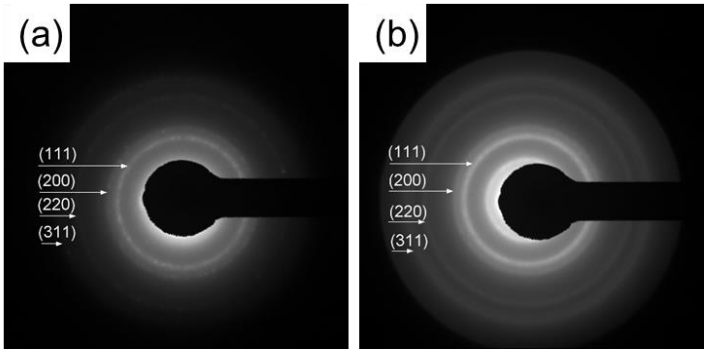

Figure 2-8. SAED patterns of PtNi/MWCNTs prepared with (a) $Ni[Tf_2N]_2$ and (b) $Ni(acac)_2$ at the sampling point L depicted in Figure 2-1.

which can be divided into two categories: (I) when T_{Pt} is lower than T_{Ni} and (II) when T_{Pt} is higher than T_{Ni}. For category (i), such as the combination of $Pt(acac)_2$ and $Ni[Tf_2N]_2$, Pt nanoparticles were first generated at lower temperatures and served as the seeds for Ni deposition at higher heating temperatures. Eventually, PtNi alloy solid solution nanoparticles with an fcc crystal structure were produced, likely via Pt-rich core Ni or patch-like Ni shell

nanoparticle formation. Such an assertion is supported by the absence of clear peak shifts in the XRD patterns of Pt in some specimens, even when the Ni contents in the PtNi/MWCNTs exceeded ca. 30 at%. For category (ii), such as the combination of $Pt(acac)_2$ and $Ni(acac)_2$, as shown in Figure 2-6, Ni-rich PtNi alloy nanoparticle production occurred at the onset of heating at 573 K due to the lower nanoparticle formation temperature of Ni ($T_{Ni} < T_{Pt}$). However, the PtNi alloy nanoparticles shifted from Ni-rich to Pt-rich upon further heating due to the slower Pt deposition step. In summary, I can depict the schematic illustration of the plausible PtNi alloy formation mechanisms as shown in Figure 2-9.

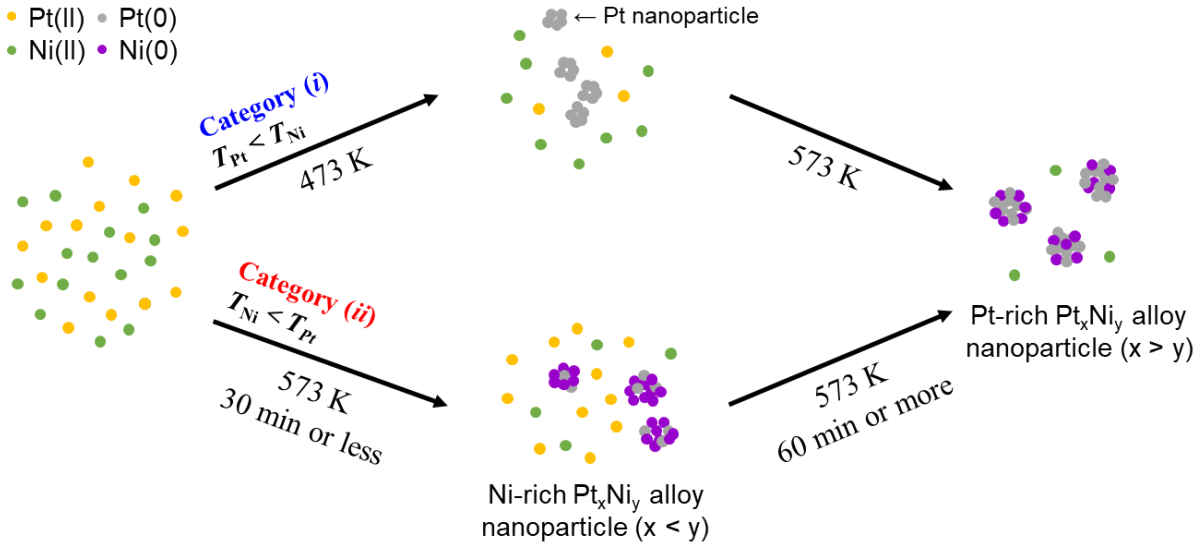

Figure 2-9. Schematic illustration of plausible PtNi alloy formation mechanisms derived from the detailed analyses of the PtNi/MWCNTs prepared by the staircase heating process.

Table 2-1. Summary of PtNi/MWCNTs prepared in the $[N_{1,1,1,3}][Tf_2N]$ with 5 mmol L^{-1} $Pt(acac)_2$, 5 mmol L^{-1} $Ni[Tf_2N]_2$, and 1.25 g L^{-1} MWCNT in this chapter.

Sampling point	Condition	Mean particle size / nm	Pt loading amount / wt%	Ni content in nanoparticles / at%	ECSA / m^2 g^{-1}	Current density at 0.90 V / mA cm^{-2}
C	473 K	1.0 (0.3) [a]	1.0	0	-	-
D	473 K, 1h	1.9 (0.6) [a]	12.5	4	-	-
E	573 K	2.4 (0.5) [a]	26.4	6	46.1	0.397
I	573 K, 1h	2.7 (0.4) [a]	28.7	18	80.0	0.895
J	573 K, 2h	2.8 (0.4) [a]	27.0	26	66.2	1.102
K	573 K, 3h	2.4 (0.5) [a]	26.6	34	46.8	1.431
L	573 K, 4h	2.6 (0.5) [a]	23.3	30	50.8	2.123

[a] The values in parentheses are standard deviations.

Table 2-2. Summary of PtNi/MWCNTs prepared in the $[N_{1,1,1,3}][Tf_2N]$ with 5 mmol L^{-1} $Pt(acac)_2$, 5 mmol L^{-1} $Ni(acac)_2$, and 1.25 g L^{-1} MWCNT in this chapter.

Sampling point	Condition	Mean particle size / nm	Pt loading amount / wt%	Ni content in nanoparticles / at%	ECSA / m^2 g^{-1}	Current density at 0.90 V / mA cm^{-2}
E	573 K	1.1 (0.3) [a]	-	-	-	-
F	573 K, 5 min	1.3 (0.4) [a]	3.3	88	23.2	0.020
G	573 K, 15 min	1.8 (0.5) [a]	12.1	53	46.4	0.069
H	573 K, 30 min	2.0 (0.8) [a]	18.7	47	76.9	0.255
I	573 K, 1h	2.8 (0.6) [a]	25.8	30	55.3	1.546
J	573 K, 2h	3.5 (0.6) [a]	29.1	35	-	-
K	573 K, 3h	2.6 (0.5) [a]	27.8	32	-	-
L	573 K, 4h	3.7 (0.7) [a]	26.2	38	39.4	1.316

[a] The values in parentheses are standard deviations.

2-3-2. Electrocatalytic performance of PtNi/MWCNTs obtained in staircase heating

The PtNi alloy nanoparticle formation mechanism, which was clarified using the staircase heating process, indicates that the alloy composition and the crystal structure vary during such processes. It can be deduced that the electrocatalytic activities of the PtNi/MWCNTs for ORR also change with the particle size, alloy composition, and crystal structure of the PtNi alloy nanoparticles supported on the MWCNTs. Figure 2-10 shows cyclic voltammograms recorded using the GC electrodes with select PtNi/MWCNT samples in a N_2-saturated 0.1 M $HClO_4$ aqueous solution. Several commonly observed redox waves due to hydrogen and oxygen

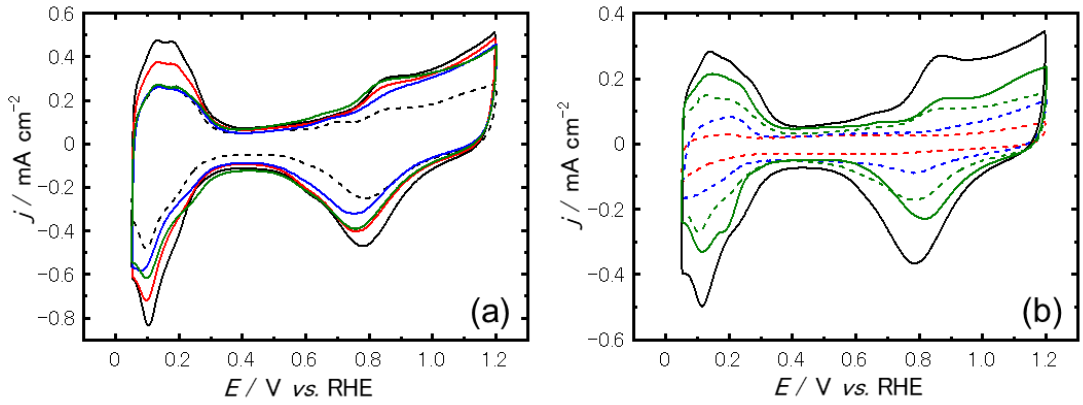

Figure 2-10. Cyclic voltammograms recorded at glassy carbon electrodes with the PtNi/MWCNTs in a N_2-saturated 0.1 M $HClO_4$ aqueous solution. The Ni precursors used for preparing the PtNi/MWCNTs were (a) $Ni[Tf_2N]_2$ and (b) $Ni(acac)_2$. The sampling points during the staircase heating process were (- - -) E, (- - -) F, (- - -) G, (- - -) H, (—) I, (—) J, (—) K, and (—) L. The scan rates were 10 mV s^{-1}.

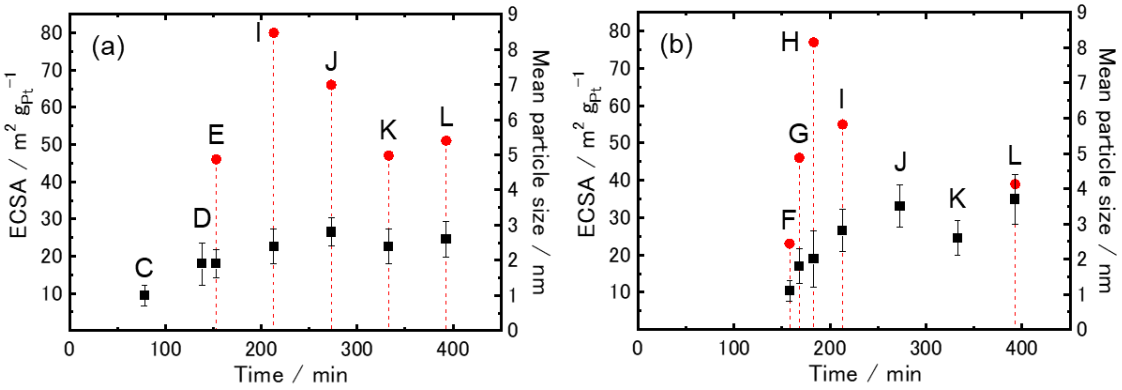

Fig. 2-11 (■) Mean particle size and (●) ECSA change of the PtNi nanoparticles in PtNi/MWCNTs prepared with (a) $Ni[Tf_2N]_2$ and (b) $Ni(acac)_2$. The sampling points during the staircase heating process are denoted on these figures.

electrochemical reactions were observed at potentials ranging from 0.10 to 0.35 V and from 0.60 to 1.00 V, respectively. ECSA data of the PtNi alloy nanoparticles are summarized in Figure 2-11, along with their corresponding mean particle size. For the PtNi/MWCNTs obtained using $Ni[Tf_2N]_2$, the highest ECSA value (80.0 $m^2\ g_{Pt}^{-1}$) was observed in the specimen taken at sampling point I. In the case of the specimens prepared from $Ni(acac)_2$, the highest ECSA value was 76.9 $m^2\ g_{Pt}^{-1}$ (sampling point H). In both cases, the ECSA values varied according to a volcano-shaped curve and seemed to be independent of the mean particle size. Such a phenomenon may have been caused by a synergetic effect of a better PtNi alloy nanoparticle dispersibility on the MWCNTs (Figure 2-2d), an appropriate Ni content in the PtNi/MWCNTs, and a favorable crystal structure for the PtNi nanoparticle.

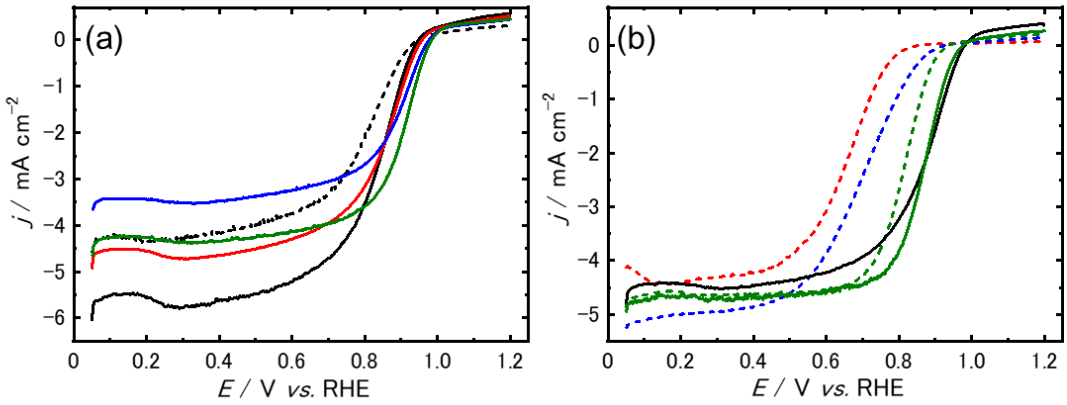

Figure 2-12. Hydrodynamic voltammograms recorded at glassy carbon electrodes with the specimens in a O_2-saturated 0.1 M $HClO_4$ aqueous solution. The Ni precursors used for preparing the PtNi/MWCNTs were (a) $Ni[Tf_2N]_2$ and (b) $Ni(acac)_2$. The sampling points during the staircase heating process were (- - -) E, (- - -) F, (- - -) G, (- - -) H, (—) I, (—) J, (—) K, and (—) L. The revolution speeds were 1600 rpm. The scan rates were 10 mV s^{-1}.

The catalytic ability of the samples for ORR was evaluated using the polarization curve of select PtNi/MWCNTs. Figure 2-12 shows the RDE-LSVs taken using the GC rotating disk electrodes with different PtNi/MWCNTs (1600 rpm) in an O_2-saturated 0.1 M $HClO_4$ aqueous solution. I observed that the current densities of the specimens produced using $Ni[Tf_2N]_2$ at 0.90 V increased with longer heating times (Figure 2-12a). A similar trend was also observed among the specimens prepared using $Ni(acac)_2$ (Figure 2-12b). In both cases, the maximum

current density was obtained with the PtNi/MWCNTs that had similar features, such as mean particle size, Pt loading amount, and Ni content in the nanoparticles. Particularly, the Ni content seemed to be an important factor. When the Ni content was approximately 30 at%, a favorable catalytic performance was attained. The binary phase diagram of Pt and Ni shows that the Pt_3Ni alloy, which has a considerably high catalytic performance,[76] was formed when the Ni content was approximately 30 at% and the temperature was 573 K.[77] Additionally, most limiting current densities for ORR shown in Figure 2-12 did not reach the commonly observed value, which is approximately −6 mA cm^{-2}. A similar decrease in the limiting current was not observed in our previous study on the IL one-pot preparation process with heating at 573 K. However, the aforementioned study did not include the heating steps at lower temperatures, 373 and 473 K.[67] It suggests that longer heating time over 4 hours and/or lower heating temperature below 473 K give some sort of negative impact to the PtNi/MWCNTs. In addition to this, thermal decomposition products derived from Ni precursors under such heating conditions may cause the undesirable ORR performance. Although I investigated the unexpected catalytic behavior, unfortunately the reason(s) could not be revealed. Despite the insufficient electrode performance, some PtNi/MWCNTs prepared in this research had a better ECSA and current density for ORR at 0.90 V, compared with those of samples previously obtained via a similar IL-based one-pot process but not the same heating process.[67] By using the staircase heating process, I was able to understand the appropriate conditions for designing PtNi/MWCNTs with a higher ORR catalytic activity using an IL one-pot process.

2-4. Conclusions

The formation mechanism of the PtNi/MWCNTs prepared via an IL one-pot process was examined using the staircase heating process with two different Ni metal precursors, $Ni[Tf_2N]_2$

and $Ni(acac)_2$. Although the final products were similar upon completion of the process, regardless of the precursor species, there was a notable composition difference between the initial steps of the PtNi nanoparticle formation, depending on the Ni precursor used. The catalytic performance of the specimens collected throughout the staircase heating process depended on the preparation conditions. In some cases, the catalytic performance was better than those of the PtNi/MWCNTs produced via the conventional heating process. Variations in the catalytic behavior strongly suggest that the heating process is crucial for controlling the characteristics of the PtNi/MWCNTs in an IL one-pot pyrolytic process. The findings reported in this article will be useful for the production of high-performance ORR electrocatalysts that can reduce Pt consumption.

Chapter 3

PtNi/MWCNTs Produced in a Nickel(II) Oxalate Dihydrate Dispersed Ionic Liquid with $Pt(acac)_2$ by One-Pot Pyrolysis Method

3-1. Introduction

For nanoparticle preparation through the widely used colloidal synthesis method and the novel IL one-pot pyrolysis method, soluble metal halides,[78, 79] nitrates,[80, 81] and acetylacetonates[82, 83] are commonly used as metal precursors, because it is common knowledge to provide a homogeneous condition for inducing smoothly chemical reactions. In Chapter 2, however, it was shown that a poorly soluble Ni precursor, $Ni(acac)_2$, was also utilizable as a precursor for one-pot preparation of PtNi/MWCNT.[84] This unexpected result may imply that the precursor can be in any state in the reaction medium as long as the species generated by thermal decomposition can contribute the nanoparticle formation. In order to further extend the applicability of the one-pot pyrolysis preparation, in this research, $NiC_2O_4{\cdot}2H_2O$, which is insoluble in most solvents including IL and has crystal water, was used as a nickel precursor. This compound was dispersed in $[N_{1,1,1,3}][Tf_2N]$ throughout the IL one-pot pyrolysis process to clarify the effect of crystal water in Ni precursor on the PtNi/MWCNT preparation. The experimental results concluded that crystal water from the insoluble metal precursor has an insignificant effect on PtNi/MWCNT preparation. The findings from the experiments concluded that the IL one-pot pyrolysis method can provide us with more choices of metal precursors in nanoparticle and its supported carbon composite preparations.

3-2. Experimental section

3-2-1. Synthesis of PtNi/MWCNTs

PtNi/MWCNT fabrication was conducted using the IL one-pot pyrolysis method under N_2 atmosphere. The reaction medium was 2 mL of $[N_{1,1,1,3}][Tf_2N]$ IL (Kanto Chemical Co., Inc.) with 5 mmol L^{-1} $Pt(acac)_2$ (Mitsuwa Chemicals Co., Ltd.), 5 mmol L^{-1} $NiC_2O_4 \cdot 2H_2O$, (Mitsuwa Chemicals Co., LLC.), and 1.25 g L^{-1} of MWCNT (Sigma-Aldrich Co., LLC.). The IL mixture was agitated at room temperature overnight to uniformly disperse the precursors and MWCNTs. A staircase heating process introduced in chapter 2 was employed for the synthesis of PtNi/MWCNT. The heating process will be graphically explained later. The synthesized PtNi/MWCNTs were rinsed with anhydrous acetonitrile multiple times and dried under a vacuum overnight.

3-2-2. Characterization

Characterization of the Pt/MWCNTs were carried out in the same method as in chapter 1.

3-3. Results and discussion

3-3-1. Thermogravimetric (TG) analysis of the metal precursors

The thermal stability of $Pt(acac)_2$, $NiC_2O_4 \cdot 2H_2O$, and $[N_{1,1,1,3}][Tf_2N]$ was examined by TG analysis before preparing the PtNi/MWCNT composite using the IL one-pot pyrolysis method (Figure 3-1). For $Pt(acac)_2$ and $[N_{1,1,1,3}][Tf_2N]$, simple one-step thermal degradation was recognized. In contrast, $NiC_2O_4 \cdot 2H_2O$ was decomposed by a two-step process. The reactions at the first and second steps were attributed to anhydrous nickel(II) oxalate (NiC_2O_4) formation and NiC_2O_4 thermal decomposition, respectively, leading to Ni metal deposition.[85, 86] $[N_{1,1,1,3}][Tf_2N]$ IL was confirmed as a viable reaction medium for the IL-based pyrolysis method when the heating temperature was less than ca. 650 K. Considering these results and a

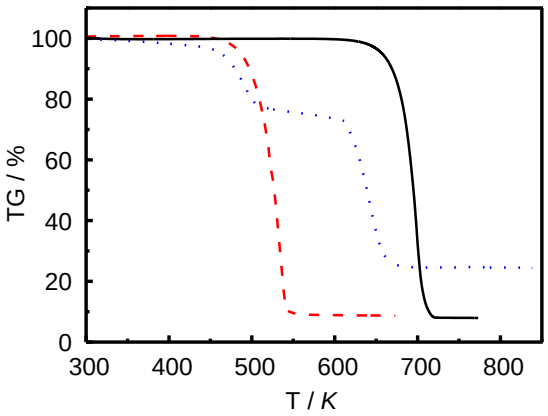

Figure 3-1. TG measurement results of (—) $[N_{1,1,1,3}][Tf_2N]$, (- - -) $Pt(acac)_2$, (· · ·) $NiC_2O_4{\cdot}2H_2O$,. The measurements were conducted at 10 K min^{-1} under a dry N_2 atmosphere.

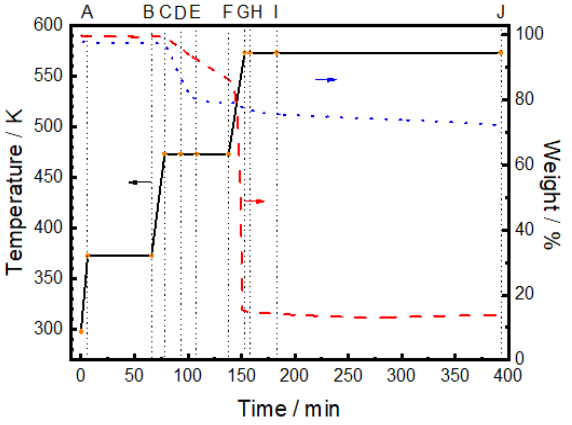

Figure 3-2. (—) Heating profile employed for the staircase heating process and TG measurement results of (- - -) $Pt(acac)_2$, (· · ·) and $NiC_2O_4{\cdot}2H_2O$ obtained using the staircase heating process. Samples were taken from the IL mixtures containing the metal precursors and MWCNTs at points A–J as shown on the top axis.

recent finding,[84] I applied a staircase heating process with three temperature plateaus at 373 K, 473 K, and 573 K to the one-pot pyrolysis method because the nanoparticle formation can be readily controlled by this approach. The heating conditions are graphically depicted in Figure 3-2 and were employed for the TG analysis. As shown in Figure 3-2, the weight loss for $Pt(acac)_2$ resulting from Pt deposition was initiated at 473 K, and with increasing heating time, it became clearer than that observed through the standard TG analysis (Figure 3-1). Consequently, the weight loss was completed at the beginning of the plateau at 573 K. Thermal decomposition of metal precursors in $[N_{1,1,1,3}][Tf_2N]$ would be kinematically prohibited by the standard TG analysis owing to the rapid temperature change. Dehydration of $NiC_2O_4{\cdot}2H_2O$ was observed at the beginning of the plateau at 473 K. Slight weight loss continued throughout the heating. In the plateau at 573 K, $NiC_2O_4{\cdot}2H_2O$ exhibited a constant weight loss. These behaviors are very similar to those for nickel bis(trifluoromethanesulfonyl)amide $(Ni[Tf_2N]_2)$ showing thermal stability over $Pt(acac)_2$.[84]

3-3-2. Characterization of PtNi/MWCNTs obtained in the staircase heating process

Figure 3-3 shows TEM images of the specimens prepared in the $[N_{1,1,1,3}][Tf_2N]$ mixtures with $NiC_2O_4{\cdot}2H_2O$ as the Ni precursor. The specimens were taken from the IL mixture after different heating processes, labeled A-J in Figure 3-2. Measurable nanoparticles were confirmed only under the heating conditions at 573 K, i.e., conditions G-J. The mean particle sizes of the nanoparticles deposited on the MWCNTs are summarized in Table 3-1. A

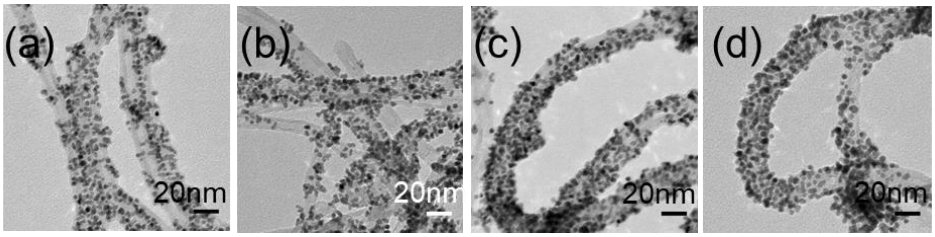

Figure 3-3. TEM images of Pt-Ni/MWCNTs prepared in the $[N_{1,1,1,3}][Tf_2N]$ with 5 mmol L^{-1} $Pt(acac)_2$, 5 mmol L^{-1} $NiC_2O_4{\cdot}2H_2O$, and 1.25 g L^{-1} MWCNT. Samplings of the IL mixture were conducted at the sampling points of (a) G, (b) H, (c) I, (d) J depicted in Figure 3-2.

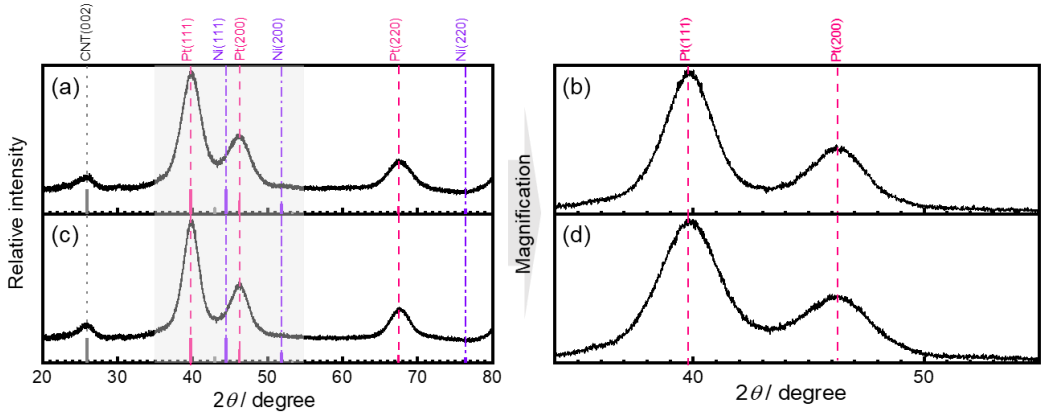

Figure 3-4. X-ray diffraction patterns of the PtNi/MWCNTs prepared at sampling point (a, b) G and (c, d) J. The reflections from Pt metal (ICDD No.00-04-0802), Ni metal (ICDD No.00-04-0850) and carbon nanotube (ICDD No.00-058-1638) are denoted at the bottom of the figure. (b) and (d) were the magnified figures for the light blue area in figures (a) and (c).

considerable number of nanoparticles with mean particle sizes of 3.7–4.4 nm were observed. Given the results of standard TG analysis for the metal precursors (Figure 3-1), the Ni content of the specimens should be significantly lower than the Pt content. Contrary to our expectation, ICP-AES results of the specimens obtained under conditions G and J show that the Ni content

of the specimens was >25 at%, which is identical to that of the Pt_3Ni alloy exhibiting considerably high catalytic activity.[67] This unexpected result was also recognized when $Ni[Tf_2N]_2$ was employed as a nickel precursor.[84] It seems to be a common thread in nickel precursors that have thermal stability over $Pt(acac)_2$. The PtNi/MWCNT prepared under condition G showed a higher Ni content than that under condition J, possibly because of the unreacted $NiC_2O_4 \cdot 2H_2O$ involved in the specimen.

XRD patterns of the as-prepared PtNi/MWCNTs at point G and J are shown in Figure 3-4 and are almost identical to those of the Pt metal. However, the XRD patterns shift very slightly to a higher angle (Figure 3-4b and 3-4d), suggesting that the PtNi alloy nanoparticle with a face-centered cubic solid solution phase is formed under the experimental condition.[73] Importantly, crystal water contained in the Ni precursor had an insignificant effect on the PtNi/MWCNT preparation through the IL one-pot pyrolysis method. This method did not need rigorous moisture control throughout the heating process because of the strong hydrophobicity of the $[N_{1,1,1,3}][Tf_2N]$ IL.[87]

Table 3-1. Summary of PtNi/MWCNTs prepared in $[N_{1,1,1,3}][Tf_2N]$ with 5 mmol L^{-1} $Pt(acac)_2$, 5 mmol L^{-1} $NiC_2O_4 \cdot 2H_2O$, and 1.25 g L^{-1} MWCNT in this chapter.

Sampling point	Condition	Size / nm	Pt loading amount / wt%	Ni content in nanoparticles at%
G	300 K	3.7 (0.7)[a]	25.5	34.9
H	300K, 5min	3.9 (0.7)[a]	-	-
I	300 K, 1 h	4.1 (0.8)[a]	-	-
J	300K , 4 h	4.4 (0.8)[a]	23.5	25.6

[a] The values in parentheses are standard deviations.

3-4. Conclusions

PtNi/MWCNTs were successfully prepared by the IL one-pot pyrolysis method using the staircase heating process with an insoluble Ni metal precursor with crystal water, $NiC_2O_4 \cdot 2H_2O$. The use of $NiC_2O_4 \cdot 2H_2O$ has negligible effect on the mean particle size, the Ni content of the nanoparticles, or crystal structure. This indicates that the solubility and existence of crystal water are not significant for a metal precursor used in the one-pot pyrolysis method to prepare metal and alloy nanoparticles. It is quite different from other chemical reactions in IL which requires the homogeneous condition without contamination. The application of this one-pot pyrolysis method is extended by the use of a different metal precursor. Therefore, by making full use of this method, I could prepare the metal and alloy nanoparticles, and their supported carbon materials, which are difficult to synthesize using the conventional methods.

Summary

As described in this thesis, the PtNi/MWCNT with high electrocatalytic performance were successfully synthesized utilizing the one-pot pyrolysis method. The effect of Ni proportion variation on the electrocatalytic performance of PtNi/MWCNT catalyst and the PtNi nanoparticle formation mechanism dependent on different Ni precursors were discussed in each chapter. The main results and conclusions obtained in this study are summarized as follows:

In chapter 1, the electrocatalytic performance for the PtNi/MWCNT catalyst obtained from one-pot pyrolysis method was described. It was found that all the prepared electrocatalysts showed better durability than that of a commercially available one. Both the chemically inert nature of the MWCNTs and the existence of the thin IL layer between the Pt nanoparticles and the carbon support suppress carbon corrosion and lead to favorable results. The bell-shaped curve constructed in this chapter allows us to predict the mass activity of the PtNi/MWCNTs from the Ni content in the PtNi alloy nanoparticles.

In chapter 2, the formation mechanism of the PtNi/MWCNTs prepared via an IL one-pot process was illustrated via comparison between two different Ni metal precursors, $Ni[Tf_2N]_2$ and $Ni(acac)_2$. Although the final products were similar upon completion of the process, regardless of the precursor species, there was a notable difference between the initial steps of the PtNi nanoparticle formation, depending on the Ni precursor used. Variations in the catalytic behavior strongly suggest that the heating process is crucial for controlling the characteristics of the PtNi/MWCNTs in an IL one-pot pyrolysis process.

In Chapter 3, it was described that this one-pot pyrolysis method could be further applied to an insoluble Ni metal precursor with crystal water, $NiC_2O_4 \cdot 2H_2O$. The use of $NiC_2O_4 \cdot 2H_2O$ has negligible effect on the mean particle size, the Ni content of the nanoparticles, and crystal structure. This indicates that the solubility and existence of crystal water are not significant for a metal precursor used in the one-pot pyrolysis method to prepare metal and alloy nanoparticles. The application of this one-pot pyrolysis method is extended by the use of a different metal precursor.

List of Publications

1. Platinum and PtNi nanoparticle-supported multiwalled carbon nanotube electrocatalysts prepared by one-pot pyrolytic synthesis with an ionic liquid

   Yu Yao, Reiko Izumi, Tetsuya Tsuda, Yoshifumi Oshima, Akihito Imanishi, Naoko Oda, and Susumu Kuwabata

   ACS Applied Energy Materials, **2019**, *2*, 4865-4872.

2. One-pot synthesis of PtNi alloy nanoparticle-supported MWCNTs in an ionic liquid using a staircase heating process

   Yu Yao, Reiko Izumi, Tetsuya Tsuda, and Susumu Kuwabata

   ACS Omega, *submitted.*

3. PtNi alloy nanoparticle-supported MWCNTs produced in a nickel(II) oxalate dehydrate dispersed ionic liquid with $Pt(acac)_2$ by one-pot pyrolysis method

   Yu Yao, Qingning Xiao, Tetsuya Tsuda, and Susumu Kuwabata

   Electrochemistry, *accepted.*

4. Platinum Nanoparticle-Supported sp^2 Carbon Electrocatalysts Synthesized by an Ionic Liquid-Based One-Pot Pyrolysis Method

   Yu Yao, Qingning Xiao, Tetsuya Tsuda, and Susumu Kuwabata

   In preparation

List of Supplementary Publications

1. Pt nanoparticle-supported carbon electrocatalysts functionalized with protic ionic liquid and organic salt
   Reiko Izumi, Yu Yao, Tetsuya Tsuda, Tsukasa Torimoto, and Susumu Kuwabata
   Advanced Materials Interfaces, **2018**, *5,* 1701123/1-5.

2. Oxygen reduction electrocatalysts sophisticated by using Pt nanoparticle-dispersed ionic liquids with electropolymerizable additives
   Reiko Izumi, Yu Yao, Tetsuya Tsuda, Tsukasa Torimoto, and Susumu Kuwabata
   Journal of Materials Chemistry A, **2018**, *6,* 11853-11862.

3. Platinum Nanoparticle-supported Electrocatalysts Functionalized by Carbonization of a Protic Ionic Liquid and Organic Salt
   Reiko Izumi, Yu Yao, Tetsuya Tsuda, Tsukasa Torimoto, and Susumu Kuwabata
   ACS Applied Energy Materials, **2018**, *1,* 3030-3034.

References

[1] L. Chong, J.G. Wen, J. Kubal, F.G. Sen, J.X. Zou, J. Greeley, M. Chan, H. Barkholtz, W.J. Ding, D.J. Liu, *Science*, **2018**, *362*, 1276-1281.

[2] M.F. Li, Z.P. Zhao, T. Cheng, A. Fortunelli, C.Y. Chen, R. Yu, Q.H. Zhang, L. Gu, B.V. Merinov, Z.Y. Lin, E.B. Zhu, T. Yu, Q.Y. Jia, J.H. Guo, L. Zhang, W.A. Goddard, Y. Huang, X.F. Duan, *Science*, **2016**, *354*, 1414-1419.

[3] S. Sui, X.Y. Wang, X.T. Zhou, Y.H. Su, S. Riffatc, C.J. Liu, *J. Mater. Chem. A*, **2017**, *5*, 1808-1825.

[4] H.S. Oh, H. Kim, *J. Power Sources*, **2012**, *212*, 220-225.

[5] J.A. Varnell, E.C.M. Tse, C.E. Schulz, T.T. Fister, R.T. Haasch, J. Timoshenko, A.I. Frenkel, A.A. Gewirth, *Nat. Commun.*, **2016**, *7*.

[6] D.H. Youn, G. Bae, S. Han, J.Y. Kim, J.W. Jang, H. Park, S.H. Choi, J.S. Lee, *J. Mater. Chem. A*, **2013**, *1*, 8007-8015.

[7] K. Waki, R.A. Wong, H.S. Oktaviano, T. Fujio, T. Nagai, K. Kimoto, K. Yamada, *Energy Environ. Sci.*, **2014**, *7*, 1950-1958.

[8] J.K. Norskov, J. Rossmeisl, A. Logadottir, L. Lindqvist, J.R. Kitchin, T. Bligaard, H. Jonsson, *J. Phys. Chem. B*, **2004**, *108*, 17886-17892.

[9] V.R. Stamenkovic, B.S. Mun, M. Arenz, K.J.J. Mayrhofer, C.A. Lucas, G.F. Wang, P.N. Ross, N.M. Markovic, *Nat. Mater.*, **2007**, *6*, 241-247.

[10] Q. Li, L.H. Wu, G. Wu, D. Su, H.F. Lv, S. Zhang, W.L. Zhu, A. Casimir, H.Y. Zhu, A. Mendoza-Garcia, S.H. Sun, *Nano Lett.*, **2015**, *15*, 2468-2473.

[11] K.A. Kuttiyiel, Y. Choi, S.-M. Hwang, G.-G. Park, T.-H. Yang, D. Su, K. Sasaki, P. Liu, R.R. Adzic, *Nano Energy*, **2015**, *13*, 442-449.

[12] W. Xiao, J. Zhu, L. Han, S. Liu, J. Wang, Z. Wu, W. Lei, C. Xuan, H.L. Xin, D. Wang, *Nanoscale*, **2016**, *8*, 14793-14802.

[13] Q. Jia, K. Caldwell, K. Strickland, J.M. Ziegelbauer, Z. Liu, Z. Yu, D.E. Ramaker, S. Mukerjee, *ACS Catal.*, **2014**, *5*, 176-186.

[14] M. Oezaslan, H. Frédéric, S. Peter, *J. Electrochem. Soc.*, **2012**, *159*, B444-B454.

[15] S. Mezzavilla, C. Baldizzonev, A.C. Swertz, N. Hodnik, E. Pizzutilo, G. Polymeros, G.P. Keeley, J. Knossalla, M. Heggen, K.J.J. Mayrhofer, F. Schuth, *ACS Catal.*, **2016**, *6*, 8058-8068.

[16] X. Huang, Z. Zhao, L. Cao, Y. Chen, E. Zhu, Z. Lin, M. Li, A. Yan, A. Zettl, Y.M. Wang, *Science*, **2015**, *348*, 1230-1234.

[17] J.R. Kitchin, J.K. Norskov, M.A. Barteau, J.G. Chen, *Phys. Rev. Lett.*, **2004**, *93*, 156801.

[18] S. Rudi, X. Tuaev, P. Strasser, *Electrocatalysis*, **2012**, *3*, 265-273.

[19] Y.J. Wang, D.P. Wilkinson, J.J. Zhang, *Chem. Rev.*, **2011**, *111*, 7625-7651.

[20] A. Moisala, Q. Li, I.A. Kinloch, A.H. Windle, *Compos. Sci. Technol.*, **2006**, *66*, 1285-1288.

[21] J.H. Seol, I. Jo, A.L. Moore, L. Lindsay, Z.H. Aitken, M.T. Pettes, X.S. Li, Z. Yao, R. Huang, D. Broido, N. Mingo, R.S. Ruoff, L. Shi, *Science*, **2010**, *328*, 213-216.

[22] X. Wang, W.Z. Li, Z.W. Chen, M. Waje, Y.S. Yan, *J. Power Sources*, **2006**, *158*, 154-159.

[23] X.J. Zhou, J.L. Qiao, L. Yang, J.J. Zhang, *Adv. Energy Mater.*, **2014**, *4*, 1301523.

[24] A. Peigney, C. Laurent, E. Flahaut, R.R. Bacsa, A. Rousset, *Carbon*, **2001**, *39*, 507-514.

[25] Y.W. Zhu, S. Murali, M.D. Stoller, K.J. Ganesh, W.W. Cai, P.J. Ferreira, A. Pirkle, R.M. Wallace, K.A. Cychosz, M. Thommes, D. Su, E.A. Stach, R.S. Ruoff, *Science*, **2011**, *332*, 1537-1541.

[26] B.M. Quinn, C. Dekker, S.G. Lemay, *J. Am. Chem. Soc.*, **2005**, *127*, 6146-6147.

[27] L.T. Qu, L.M. Dai, *J. Am. Chem. Soc.*, **2005**, *127*, 10806-10807.

[28] K.R. Reddy, B.C. Sin, K.S. Ryu, J.C. Kim, H. Chung, Y. Lee, *Synthetic Met.*, **2009**, *159*,

595-603.

[29] M. Okamoto, T. Fujigaya, N. Nakashima, *Small*, **2009**, *5*, 735-740.

[30] C.L. Sun, L.C. Chen, M.C. Su, L.S. Hong, O. Chyan, C.Y. Hsu, K.H. Chen, T.F. Chang, L. Chang, *Chem. Mater.*, **2005**, *17*, 3749-3753.

[31] T. Torimoto, K. Okazaki, T. Kiyama, K. Hirahara, N. Tanaka, S. Kuwabata, *Appl. Phys. Lett.*, **2006**, *89*, 243177.

[32] K. Okazaki, T. Kiyama, T. Suzuki, S. Kuwabata, T. Torimoto, *Chem. Lett.*, **2009**, *38*, 330-331.

[33] S. Kuwabata, T. Tsuda, T. Torimoto, *J. Phys. Chem. Lett.*, **2010**, *1*, 3177-3188.

[34] K. Yoshii, T. Tsuda, T. Arimura, A. Imanishi, T. Torimoto, S. Kuwabata, *RSC Adv.*, **2012**, *2*, 8262-8264.

[35] M. Hirano, K. Enokida, K. Okazaki, S. Kuwabata, H. Yoshida, T. Torimoto, *Phys. Chem. Chem. Phys.*, **2013**, *15*, 7286-7294.

[36] T. Tsuda, T. Kurihara, Y. Hoshino, T. Kiyama, K. Okazaki, T. Torimoto, S. Kuwabata, *Electrochemistry*, **2009**, *77*, 693-695.

[37] T. Tsuda, K. Yoshii, T. Torimoto, S. Kuwabata, *J. Power Sources*, **2010**, *195*, 5980-5985.

[38] K. Yoshii, K. Yamaji, T. Tsuda, H. Matsumoto, T. Sato, R. Izumi, T. Torimoto, S. Kuwabata, *J. Mater. Chem. A*, **2016**, *4*, 12152-12157.

[39] R. Izumi, Y. Yao, T. Tsuda, T. Torimoto, S. Kuwabata, *Adv. Mater. Interfaces*, **2018**, *5*, 1701123.

[40] R. Izumi, Y. Yao, T. Tsuda, T. Torimoto, S. Kuwabata, *J. Mater. Chem. A*, **2018**, *6*, 11853-11862.

[41] R. Izumi, Y. Yao, T. Tsuda, T. Torimoto, S. Kuwabata, *ACS Appl. Energy Mater.*, **2018**, *1*, 3030-3034.

[42] V.R. Stamenkovic, B. Fowler, B.S. Mun, G.F. Wang, P.N. Ross, C.A. Lucas, N.M.

Markovic, *Science*, **2007**, *315*, 493-497.

[43] Y.G. Suo, L. Zhuang, J.T. Lu, *Angew. Chem. Int. Edit.*, **2007**, *46*, 2862-2864.

[44] M. Shao, J.H. Odell, A. Peles, D. Su, *Chem. Commun.*, **2014**, *50*, 2173-2176.

[45] V. Čolić, A.S. Bandarenka, *ACS Catal.*, **2016**, *6*, 5378-5385.

[46] M. Asano, R. Kawamura, R. Sasakawa, N. Todoroki, T. Wadayama, *ACS Catal.*, **2016**, *6*, 5285-5289.

[47] M.J. Earle, U. Hakala, B.J. McAuley, M. Nieuwenhuyzen, A. Ramani, K.R. Seddon, *Chem. Commun.*, **2004**, 1368-1369.

[48] T. Katase, S. Imashuku, K. Murase, T. Hirato, Y. Awakura, *Sci. Technol. Adv. Mat.*, **2006**, *7*, 502-510.

[49] K. Yamamoto, D. Kolb, R. Kötz, G. Lehmpfuhl, *J. Electroanal. Chem. Interfacial Electrochem.*, **1979**, *96*, 233-239.

[50] Fuel Cell Commercialization Conference of Japan (FCCJ), Proposals of the development targets, research and development challenges and evaluations methods concerning PEFCs, http://fcc.jp/pdf/23_01_kt.pdf.

[51] A.Z. Rubezhov, *Platinum Metals Rev.*, **1992**, *36*, 26-33.

[52] F. Jasim, I. Hamid, *Thermochim. Acta.*, **1985**, *93*, 65-68.

[53] A.J. Bard, L.R. Faulkner, Electrochemical Methods: Fundamentals and Applications, 2nd ed., John Wiley & Sons, New York, USA, 2001.

[54] T. Toda, H. Igarashi, H. Uchida, M. Watanabe, *J. Electrochem. Soc.*, **1999**, *146*, 3750-3756.

[55] Y. Shao, G. Yin, Y. Gao, *J. Power Sources*, **2007**, *171*, 558-566.

[56] T. Ioroi, T. Akita, M. Asahi, S.-i. Yamazaki, Z. Siroma, N. Fujiwara, K. Yasuda, *J. Power Sources*, **2013**, *223*, 183-189.

[57] J. Kim, S.W. Lee, C. Carlton, Y. Shao-Horn, *Electrochem. Solid-State Lett.*, **2011**, *14*,

B110-B113.

[58] J. Greeley, I.E.L. Stephens, A.S. Bondarenko, T.P. Johansson, H.A. Hansen, T.F. Jaramillo, J. Rossmeisl, I. Chorkendorff, J.K. Norskov, *Nat. Chem.*, **2009**, *1*, 552-556.

[59] Y. Zhao, L.Z. Fan, H.Z. Zhong, Y.F. Li, S.H. Yang, *Adv. Funct. Mat.*, **2007**, *17*, 1537-1541.

[60] J.J. Burk, S.K. Buratto, *J. Phys. Chem. C*, **2013**, *117*, 18957-18966.

[61] Y. Wang, A.S. Hall, *ACS Energy Lett.*, **2020**, *5*, 17-22.

[62] F. Bonet, V. Delmas, S. Grugeon, R.H. Urbina, P.Y. Silvert, K. Tekaia-Elhsissen, *Nanostruct. Mater.*, **1999**, *11*, 1277-1284.

[63] E.V. Shevchenko, D.V. Talapin, A.L. Rogach, A. Kornowski, M. Haase, H. Weller, *J. Am. Chem. Soc.*, **2002**, *124*, 11480-11485.

[64] Y.Y. Mu, H.P. Liang, J.S. Hu, L. Jiang, L.J. Wan, *J. Phys. Chem. B*, **2005**, *109*, 22212-22216.

[65] J.S. Kanady, P. Leidinger, A. Haas, S. Titlbach, S. Schunk, K. Schierle-Arndt, E.J. Crumlin, C.H. Wu, A.P. Alivisatos, *J. Am. Chem. Soc.*, **2017**, *139*, 5672-5675.

[66] A. Zaleska-Medynska, M. Marchelek, M. Diak, E. Grabowska, *Adv. Colloid. Interfac.*, **2016**, *229*, 80-107.

[67] Y. Yao, R. Izumi, T. Tsuda, Y. Oshima, A. Imanishi, N. Oda, S. Kuwabata, *ACS Appl. Energy Mater.*, **2019**, *2*, 4865-4872.

[68] H.M. Wu, D. Wexler, G.X. Wang, *J. Alloy. Compd.*, **2009**, *488*, 195-198.

[69] R.S. Li, Z. Wei, T. Huang, A.S. Yu, *Electrochim. Acta.*, **2011**, *56*, 6860-6865.

[70] E.C. Wegener, Z.W. Wu, H.T. Tseng, J.R. Gallagher, Y. Ren, R.E. Diaz, F.H. Ribeiro, J.T. Miller, *Catal. Today*, **2018**, *299*, 146-153.

[71] D. Raciti, J. Kubal, C. Ma, M. Barclay, M. Gonzalez, M.F. Chi, J. Greeley, K.L. More, C. Wang, *Nano Energy*, **2016**, *20*, 202-211.

[72] K. Kusada, H. Kobayashi, R. Ikeda, Y. Kubota, M. Takata, S. Toh, T. Yamamoto, S. Matsumura, N. Sumi, K. Sato, K. Nagaoka, H. Kitagawa, *J. Am. Chem. Soc.*, **2014**, *136*, 1864-1871.

[73] C.T. Fan, G.L. Wang, L.L. Zou, J.H. Fang, Z.Q. Zou, H. Yang, *J. Power Sources*, **2019**, *429*, 1-8.

[74] Y. Liu, W. Kou, X. Li, C. Huang, R. Shui, G. He, *Small*, **2019**, *15*.

[75] X.H. Qi, X.C. Li, B. Chen, H.L. Lu, L. Wang, G.H. He, *ACS Appl. Mater. Interfaces*, **2016**, *8*, 1922-1928.

[76] X.Q. Huang, Z.P. Zhao, L. Cao, Y. Chen, E.B. Zhu, Z.Y. Lin, M.F. Li, A.M. Yan, A. Zettl, Y.M. Wang, X.F. Duan, T. Mueller, Y. Huang, *Science*, **2015**, *348*, 1230-1234.

[77] H. Okamoto, Phase Digrams for Binary Alloys, 2nd ed., ASM International, Materials Park, OH, 2010.

[78] T.W. Chen, J.X. Kang, D.F. Zhang, L. Guo, *RSC Adv.*, **2016**, *6*, 71501-71506.

[79] L.L. Zou, J. Fan, Y. Zhou, C.M. Wang, J. Li, Z.Q. Zou, H. Yang, *Nano Res.*, **2015**, *8*, 2777-2788.

[80] Y.J. Wang, J.B. Zang, L. Dong, H. Pan, Y.G. Yuan, Y.H. Wang, *Electrochim. Acta.*, **2013**, *113*, 583-590.

[81] G.R. Zhang, S. Wollner, *Appl. Catal B-Environ.*, **2018**, *222*, 26-34.

[82] H.Z. Yang, J. Zhang, S. Kumar, H.J. Zhang, R.D. Yang, J.Y. Fang, S.Z. Zou, *Electrochem. Commun.*, **2009**, *11*, 2278-2281.

[83] S.W. Chou, Y.R. Lai, Y.Y. Yang, C.Y. Tang, M. Hayashi, H.C. Chen, H.L. Chen, P.T. Chou, *J. Catal.*, **2014**, *309*, 343-350.

[84] Y. Yao, R. Izumi, T. Tsuda, S. Kuwabata, 10th Japanense Symposium on Ionic Liquids, Osaka, Japan, 2019, 1O03,

[85] B. Malecka, A. Malecki, E. Drozdz-Ciesla, L. Tortet, P. Llewellyn, F. Rouquerol,

Thermochim. Acta., **2007**, *466*, 57-62.

[86] R. Majumdar, P. Sarkar, U. Ray, M.R. Mukhopadhyay, *Thermochim. Acta.*, **1999**, *335*, 43-53.

[87] P. Wasserscheid, T. Welton, Ionic Liquids in Synthesis, Second Edition ed., Wiley-VCH, Weinheim, 2008.

Acknowledgement

First of all, the author would like to express her sincerest gratitude to Prof. Dr. Susumu Kuwabata, Department of Applied Chemistry, Graduate School of Engineering, Osaka University, for his continuous guidance, kind suggestions and warm encouragement throughout this work. The author would like to thank to Prof. Dr. Ken-ichi Nakayama and Prof. Dr. Norimitsu Tohnai for their reviewing this thesis with valuable comments and suggestions.

The author also wishes to express her special thanks to Associate Prof. Dr. Tetsuya Tsuda for his continuous guidance, invaluable suggestions, and fruitful discussion throughout this work. The author would like to express her thanks to Assistant Prof. Dr. Taro Uematsu for his valuable comments and helpful supports. The author is deeply grateful to Cross-Appointment Associate Prof. Dr. Hajime Matsumoto, Department of Energy Environment, Research Institute of Electrochemical Energy, National Institute of Advanced Industrial Science and Technology, for his warm discussions and valuable guidance. The author thanks pre-secretary, Ms. Michiko Ebukuro and secretary Miyuki Takahama for hearty supports throughout life in the laboratory. The author is indebted to Dr. Kazuki Yoshii and Dr. Reiko Izumi for their kind guidance, fruitful discussions and expert comments. The author is also grateful to all member of Kuwabata laboratory for their warm supports, friendship and invaluable memories. The author gratefully appreciates the Ministry of Education, Culture, Sports, Science and Technology (MEXT) of Japanese government for their scholarship supports.

Finally, the author wishes to express her sincerest gratitude to her farther, Guoliang Yao, her mother, Guihong Yan, and her cat, Mi for their continuous encouragements and hearty supports.

July 2020

Yu Yao